



CERN-EP-2022-242
08 November 2022

Measurement of the angle between jet axes in pp collisions at $\sqrt{s} = 5.02$ TeV

ALICE Collaboration*

Abstract

This article reports measurements of the angle between differently defined jet axes in pp collisions at $\sqrt{s} = 5.02$ TeV carried out by the ALICE Collaboration. Charged particles at midrapidity are clustered into jets with resolution parameters $R = 0.2$ and 0.4 . The jet axis, before and after Soft Drop grooming, is compared to the jet axis from the Winner-Takes-All (WTA) recombination scheme. The angle between these axes, ΔR_{axis} , probes a wide phase space of the jet formation and evolution, ranging from the initial high-momentum-transfer scattering to the hadronization process. The ΔR_{axis} observable is presented for $20 < p_{\text{T}}^{\text{ch,jet}} < 100$ GeV/ c , and compared to predictions from the PYTHIA 8 and Herwig 7 event generators. The distributions can also be calculated analytically with a leading hadronization correction related to the non-perturbative component of the Collins–Soper–Sterman (CSS) evolution kernel. Comparisons to analytical predictions at next-to-leading-logarithmic accuracy with leading hadronization correction implemented from experimental extractions of the CSS kernel in Drell–Yan measurements are presented. The analytical predictions describe the measured data within 20% in the perturbative regime, with surprising agreement in the non-perturbative regime as well. These results are compatible with the universality of the CSS kernel in the context of jet substructure.

arXiv:2211.08928v2 [nucl-ex] 6 Oct 2023

© 2022 CERN for the benefit of the ALICE Collaboration.

Reproduction of this article or parts of it is allowed as specified in the CC-BY-4.0 license.

*See Appendix C for the list of collaboration members

1 Introduction

Jets play a fundamental role in the study of quantum chromodynamics (QCD). Jets form when partons (quarks and gluons) scattered in high-momentum-transfer (hard) processes fragment into lower-energy (softer) partons. The fragmentation creates a shower of partons, until the average energy per particle falls below the scale at which color-neutral hadrons emerge. Jet substructure, which studies the radiation patterns inside jets, is a prolific field in both experiment [1] and theory [2]. The large difference between the energy scale of the hard-scattered parton and the measured hadrons leaves a significant phase space for jet formation and evolution [3]. Therefore, a multitude of jet-substructure measurements probing different regions of this phase space is needed to characterize the internal substructure of jets and advance our understanding of QCD. Numerous analyses have been carried out by the ALICE [4–12], ATLAS [13–21], CMS [22–29], and LHCb [30, 31] Collaborations at the LHC, as well as at RHIC [32–34].

In this article, a novel jet-substructure observable proposed in Ref. 35 corresponding to the angle between two definitions of the axis of a jet:

$$\Delta R_{\text{axis}} \equiv \sqrt{(y_{\text{axis}1} - y_{\text{axis}2})^2 + (\varphi_{\text{axis}1} - \varphi_{\text{axis}2})^2} \quad (1)$$

is studied. Here, a given axis corresponds to a set of coordinates in the rapidity (y) and azimuth (φ) plane. This is illustrated in Fig. 1. The ‘‘Standard’’ axis is determined by clustering the jet constituents with the anti- k_T algorithm [36] and the E recombination scheme. Alternatively, the ‘‘Groomed’’ axis can be determined by first using a systematic procedure to remove the soft wide-angle radiation in the jet and then determining the axis of the anti- k_T jet (with E recombination scheme), clustering only the constituents that remain after grooming. Given the removal of soft wide-angle radiation, this quantity is less sensitive to non-perturbative effects. The grooming procedure used in this analysis is reviewed below.

A third way to define the jet axis corresponds to reclustering the jet (initially clustered with the anti- k_T algorithm and E recombination scheme) with the Cambridge–Aachen (C/A) algorithm [37, 38] ensuring that the resulting jet includes all constituents from the original jet. The C/A algorithm clusters particles exclusively based on their spatial separation (in the y – φ plane) without taking into account their energies/momenta. Thus, particles closest in distance are clustered first, which results in an angular-ordered clustering sequence. Subsequently, the constituents are recombined with the Winner-Takes-All (WTA) transverse-momentum recombination scheme [39]. This consists of going through the clustering his-

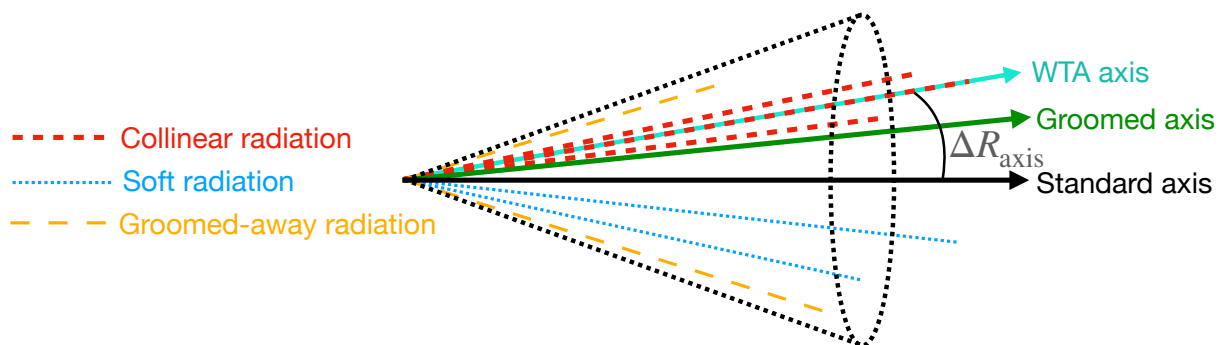


Figure 1: Representation of different jet axes. The colored dashed lines represent particles comprising the jet in the initial sample constructed with the anti- k_T algorithm and E recombination scheme. These define the ‘‘Standard’’ jet axis. The grooming procedure removes soft wide-angle radiation (represented by orange long-dashed lines), and the resulting axis (‘‘Groomed (SD)’’) is defined by the remaining particles (red dashed and blue dotted lines). Finally, the ‘‘WTA’’ axis, which is determined with all the particles in the initial (ungroomed) jet, tends to be aligned with the most-energetic particle in the jet. The ΔR_{axis} observable is determined from the angle between any pair of these axes.

tory and combining the pair of prongs in each $2 \rightarrow 1$ merging by assigning to the merged branch the direction of the harder of the two prongs and transverse momentum (p_T) corresponding to the sum of the two transverse momenta. The WTA scheme is infrared and collinear (IRC) safe and the resulting axis is insensitive to soft radiation at leading power of ΔR_{axis} , which makes it amenable to perturbative calculations [35].

The ΔR_{axis} observable is IRC safe and can be analytically calculated [35]. The sensitivity of ΔR_{axis} to non-perturbative effects can be controlled by changing the pair of axes that are used to determine the observable and also by varying the grooming and the jet resolution parameter. For instance, the difference between the Standard and Groomed axes specifically probes the influence of the groomed soft wide-angle radiation on the jet direction. Similarly, the WTA axis constitutes a robust reference against soft-radiation effects. The angle between the WTA and Standard/SD axes offers a proxy for studying how the fragmenting parton that initiated the jet gets distributed inside the jet cone. Consequently, this observable can be used both to test the performance of analytic predictions and to constrain non-perturbative models used in event generators.

The ΔR_{axis} is sensitive to Transverse-Momentum-Dependent (TMD) physics [35]. The leading hadronization correction for ΔR_{axis} is related to the non-perturbative component of the Collins–Soper–Sterman (CSS) evolution kernel or rapidity anomalous dimension. Here, leading means logarithmically enhanced in the calculation of ΔR_{axis} , in contrast to other nonperturbative components that are not logarithmically enhanced and thus expected to be small. The CSS kernel is a process-independent non-perturbative function constrained from fits to measured data that governs the non-perturbative evolution in rapidity and encodes information about soft-gluon exchanges between partons in vacuum [40]. As such, extractions from diverse physics processes such as Drell–Yan and semi-inclusive deep-inelastic scattering [41–44] should adequately describe the hadronization corrections for the jet substructure observable presented in this study. This measurement can be included in future global fits to further constrain the CSS kernel. Furthermore, it has been proposed that the CSS kernel can be determined from lattice QCD [45, 46], and such results can be benchmarked with our measurements.

The measurements presented here can also serve as a reference for measurements in heavy-ion collisions. The internal structure of jets fragmenting in the strongly interacting, deconfined state of matter formed in heavy-ion collisions is modified relative to jet fragmentation in vacuum [47, 48]. Comparing to pp collisions allows us to study the medium properties.

In this analysis, the Soft Drop grooming procedure [49] is used to determine the Groomed axis (referred to as “SD” axis from here on). The jet is first reclustered with the C/A algorithm, with the same resolution parameter used in the original clustering of the anti- k_T -based sample. This tree is then recursively declustered starting from the largest-distance splitting and at each $1 \rightarrow 2$ splitting, the condition

$$\frac{\min(p_{T,1}, p_{T,2})}{p_{T,1} + p_{T,2}} > z_{\text{cut}} \left(\frac{\Delta R_{1,2}}{R} \right)^\beta \quad (2)$$

is checked. Here, $p_{T,1}$ and $p_{T,2}$ are the transverse momenta of each prong, and $\Delta R_{1,2}$ is the angular distance between them, calculated as in Eq. 1. The jet resolution parameter is denoted by R . The free parameters z_{cut} and β determine how asymmetric and how wide the splitting can be, respectively. If the condition is not satisfied at a given splitting, the softer branch is removed from the tree and the procedure continues through the harder prong. When a splitting that satisfies the condition is found, the Soft Drop procedure stops and the branch parent to the splitting defines the groomed jet. If there is not a single splitting that satisfies the Soft Drop condition, then the grooming procedure fails. These jets are labeled “untagged” and their abundance is used in the normalization convention used in this analysis. A scan in Soft Drop parameters is carried out, both fixing $z_{\text{cut}} = 0.1$ and varying β from 0 to 3 in increments of 1 and fixing $\beta = 1$ and varying z_{cut} from 0.1 to 0.3 in increments of 0.1.

This article presents the first measurement of the ΔR_{axis} observable, which is carried out in pp collisions at a center-of-mass energy $\sqrt{s} = 5.02$ TeV with the ALICE detectors using charged-particle jets. The document is structured as follows. Section 2 describes the experimental setup used for the measurement and details of the datasets. Section 3 outlines the steps taken in the data analysis. Section 4 describes variations implemented in the analysis to determine systematic uncertainties. Section 5 presents our results and a discussion of the findings. Section 6 summarizes our findings and introduces the conclusions of this work.

2 Experimental setup and data sets

This analysis uses proton–proton (pp) collisions at $\sqrt{s} = 5.02$ TeV, recorded in 2017 with the ALICE detector at the CERN LHC [50]. A detailed description of the ALICE detector and its performance can be found in Refs. 51, 52. The event sample consists of minimum-bias events triggered by a coincidence of hits in the two V0 scintillator detectors [53], which cover an azimuthal acceptance of $0 < \varphi < 2\pi$ and pseudorapidity $2.8 < \eta < 5.1$ (V0A) and $-3.7 < \eta < -1.7$ (V0C). Pileup effects are removed by discarding events that contain multiple reconstructed vertices [54]. The primary event vertex is required to be within ± 10 cm of the nominal interaction point. The data sample contains 870 million events, corresponding to an integrated luminosity of $18.0(4)$ nb $^{-1}$ [55].

Tracks were reconstructed using the Inner Tracking System (ITS) [56] and Time Projection Chamber (TPC) [57]. The track sample consists of two track categories. In the first category, tracks are required to include at least one hit in the silicon pixel detector (SPD) of the ITS, cross at least 70 (out of 159) TPC readout pad rows, and have at least 80% of the geometrically findable space points in the TPC, among other quality criteria [58]. In the second category, tracks that do not contain any SPD hits but otherwise satisfy the track-selection criteria are refit with a constraint to the primary vertex. The inclusion of this second category produces a track sample approximately uniform in azimuth, while preserving a similar p_T resolution to tracks with SPD hits. Tracks with $p_{T,\text{track}} > 0.15$ GeV/c, $|\eta| < 0.9$, and $0 < \varphi < 2\pi$ are assigned the charged-pion mass and included in the analysis.

The ALICE detector tracking efficiency in pp collisions grows from $\approx 67\%$ at $p_{T,\text{track}} = 0.15$ GeV/c to $\approx 84\%$ at $p_{T,\text{track}} = 1$ GeV/c, and remains above $\approx 75\%$ for higher $p_{T,\text{track}}$ [51]. The track momentum resolution increases from $\approx 1\%$ at $p_{T,\text{track}} = 1$ GeV/c to $\approx 4\%$ at $p_{T,\text{track}} = 4$ GeV/c.

3 Analysis method

3.1 Jet reconstruction

Charged-particle jets were reconstructed from tracks with $0.15 < p_{T,\text{track}} < 100$ GeV/c, using the anti- k_T algorithm [36], and the E recombination scheme, for resolution parameters $R = 0.2$ and 0.4 using the FastJet package [59]. Only jets within the fiducial acceptance of the TPC ($|\eta_{\text{jet}}| < 0.9 - R$) were analyzed, and the resulting distributions are reported in four p_T^{chjet} intervals with edges at $[20, 40, 60, 80, 100]$ GeV/c. The different axes used to construct the ΔR_{axis} observable are determined from the jets in this sample. The underlying-event was not subtracted.

The jet reconstruction performance was estimated using PYTHIA 8 [60] with Monash 2013 tune [61] events (“truth” level) propagated through a GEANT 3 [62] model of the ALICE detector (“detector” level). In this sample, final-state particles are defined as those with a mean proper lifetime $c\tau > 1$ cm [63]. Particles (tracks) at truth (detector) level were individually clustered into jets, and the jets were matched between the two populations by requiring that the distance between their Standard axes in the y – φ plane satisfied $\Delta R < 0.6R$ and that the match was unique [54]. The matched jets were used to construct the jet energy scale ($\text{JES} \equiv (p_{T,\text{det}}^{\text{chjet}} - p_{T,\text{truth}}^{\text{chjet}})/p_{T,\text{truth}}^{\text{chjet}}$), jet energy resolution ($\text{JER} \equiv \sigma(p_{T,\text{det}}^{\text{chjet}})/p_{T,\text{truth}}^{\text{chjet}}$), and jet reconstruction efficiency (ϵ_{reco}), where $p_{T,\text{truth}}^{\text{chjet}}$ and $p_{T,\text{det}}^{\text{chjet}}$ refer to the transverse momentum of the

truth- and detector-level jets, respectively, and $\sigma(p_{T,\text{det}}^{\text{chjet}})$ corresponds to the standard deviation of the $p_{T,\text{det}}^{\text{chjet}}$ spectrum for a given value of $p_{T,\text{truth}}^{\text{chjet}}$. Table 1 shows values characterizing the jet-reconstruction performance. In the case of the JES, this distribution is peaked at 0, but has an asymmetric tail that shifts the mean value, Δ_{JES} , due to tracking inefficiencies. The unfolding procedure described in the next section corrects for these JES and JER effects.

Table 1: Approximate values for the figures of merit characterizing the jet-reconstruction performance in this analysis. Δ_{JES} is the mean value of the JES spectrum. See text for details.

R	p_{T}^{chjet} (GeV/ c)	Δ_{JES} (%)	JER (%)	ϵ_{reco} (%)
0.4	20	-13	21	97
	40	-16	21	100
	60	-19	22	100
	80	-21	23	100
	100	-25	24	100
0.2	20	-12	21	94
	40	-16	23	100
	60	-20	24	100
	80	-23	25	100
	100	-27	26	100

3.2 Corrections

To obtain distributions free of detector effects (truth level), the measured spectra (detector level) were unfolded using an iterative procedure based on Bayes' theorem [64, 65], implemented in the RooUnfold package [66]. This unfolding procedure accounts for effects such as track p_T resolution, tracking inefficiencies, and particle interactions in the detector volume. The input to this procedure consisted of a 4-dimensional response matrix (RM) that maps the correspondence between detector and truth levels for p_{T}^{chjet} and ΔR_{axis} . The RM was created using the simulated jets described in the previous section. The $p_{T,\text{det}}^{\text{chjet}}$ axes were constructed in the range [10, 130] GeV/ c to capture bin-migration effects. In the ΔR_{axis} cases in which one of the two axes is the SD axis, the untagged jets were included in the unfolding procedure. The unfolding iterations were fixed at the number that minimizes the quadratic sum of the statistical and systematic uncertainties. In some cases, a few more iterations were carried out until a convergence within 5% between subsequent iterations was achieved.

The unfolding procedure was validated by performing a series of closure tests. A refolding test was performed to check that the detector-level spectrum can be recovered by reversing the unfolding procedure. In this test, the unfolded result was multiplied by the response matrix and the resulting spectrum was compared to the detector-level spectrum. Additionally, a statistical-closure test was performed to confirm that the unfolding procedure is robust against statistical fluctuations in the data. In this test, the simulated detector-level spectrum was smeared by an amount equal to the statistical uncertainty of the measured data. Subsequently, the smeared spectrum was unfolded, and the agreement between the resulting distribution and the truth-level simulated distribution was assessed. Finally, a shape-closure test was performed to account for the fact that the true detector-level distribution may be different than that from the generator, and to evaluate the robustness against this shape. In this test, the shapes of the simulated detector- and truth-level spectra were scaled by the prior-scaling function described in the systematic-uncertainty section. Subsequently, the scaled detector-level spectrum was unfolded, and the resulting spectrum was compared to the scaled truth-level distribution. In all these tests, closure within the statistical uncertainties was achieved.

4 Systematic uncertainties

Three sources of systematic uncertainties are considered in this analysis: those arising from the unfolding procedure, uncertainties in the tracking efficiency, and the choice of event generator used to produce the response matrix.

The unfolding uncertainty is estimated by performing four variations of the unfolding procedure:

1. The analysis is repeated with a number of iterations varied by ± 2 around the nominal value and the average difference with respect to the nominal spectrum is taken as an uncertainty.
2. The analysis is repeated with a prior distribution multiplied by $(p_{\text{T}}^{\text{ch jet}} [\text{GeV}/c])^{\pm 0.5} \times (\pm A \Delta R_{\text{axis}} \mp B)$, where the parameters A and B are selected for each ΔR_{axis} variation such that the endpoints of the spectrum are scaled by $\approx \pm 20\%$. The maximum difference between these two variations and the nominal result is taken as an uncertainty.
3. The analysis is repeated with the transverse-momentum range $p_{\text{T,det}}^{\text{ch jet}} \in [5, 135]$ GeV/ c and the difference with respect to the nominal analysis ($p_{\text{T,det}}^{\text{ch jet}} \in [10, 130]$ GeV/ c) is taken as an uncertainty.
4. The analysis is repeated with a different ΔR_{axis} binning at detector level (slightly finer or coarser granularity) and the difference with respect to the main result is taken as an uncertainty.

Given that these four variations probe the same underlying source of uncertainty, the total unfolding uncertainty is defined as the standard deviation $\sigma_{\text{unfolding}} \equiv \sqrt{\sum_{i=1}^4 \sigma_i^2 / 4}$, where σ_i corresponds to the uncertainty from the individual variations.

The uncertainty on the ALICE tracking efficiency is 3–4%, determined by varying the track selection parameters and possible imperfections in the description of the ITS–TPC matching efficiency in the simulation. Consequently, the analysis was repeated with a RM populated with jets clustered over a track sample with 4% of all tracks randomly discarded, taking the more conservative value. Differences with respect to the nominal analysis were assigned as the systematic uncertainty due to the tracking efficiency.

To assess the model dependence of the analysis on the generated spectra used to compute the RM (based on PYTHIA 8 with Monash 2013 tune events propagated through GEANT 3), the analysis was repeated using RMs based on Herwig 7 (default tune) and PYTHIA 8 with Monash 2013 tune constructed using a fast simulation, and the difference between the two unfolded results was assigned as a systematic uncertainty. In a comparison based on PYTHIA 8 events, this fast simulation agrees with the GEANT 3-based simulation within 10%.

The total systematic uncertainty is taken as the sum in quadrature of the contributions due to the unfolding, tracking efficiency, and choice of event generator. Table 2 summarizes the range of the systematic uncertainties in different ΔR_{axis} intervals for jets of $R = 0.2$ and 0.4 in the transverse momentum range $40 < p_{\text{T}}^{\text{ch jet}} < 60$ GeV/ c . Most often, the dominant systematic uncertainty originates from the uncertainty on the tracking efficiency.

5 Results and discussion

The ΔR_{axis} distributions are reported as normalized differential cross sections:

$$\frac{1}{\sigma_{\text{jets}}(p_{\text{T}}^{\text{ch jet}})} \frac{d\sigma}{d\Delta R_{\text{axis}}} \left(p_{\text{T}}^{\text{ch jet}} \right) \equiv \frac{1}{N_{\text{jets}}(p_{\text{T}}^{\text{ch jet}})} \frac{dN}{d\Delta R_{\text{axis}}} \left(p_{\text{T}}^{\text{ch jet}} \right), \quad (3)$$

Table 2: Range of the estimated value of relative systematic uncertainties in ΔR_{axis} intervals in the transverse momentum range $40 < p_{\text{T}}^{\text{ch jet}} < 60$ GeV/c. The unfolding, tracking efficiency, and generator systematic uncertainties can be found in the columns labeled Unf., Trk. Eff., and Gen., respectively. In the case of the groomed observables, the grooming parameters are specified as (z_{cut}, β) . The displayed uncertainties correspond to the lowest and highest values for a given setting.

ΔR_{axis}	$R = 0.2$				$R = 0.4$			
	Unf.	Trk. Eff.	Gen.	Total	Unf.	Trk. Eff.	Gen.	Total
WTA–Standard	0–3%	0–8%	0–5%	1–10%	1–4%	0–6%	0–4%	1–6%
WTA–SD (0.1, 0)	1–4%	0–4%	0–3%	2–6%	1–4%	1–4%	0–4%	1–6%
WTA–SD (0.1, 1)	0–3%	0–5%	0–3%	1–5%	1–4%	0–4%	0–4%	2–6%
WTA–SD (0.1, 2)	0–2%	0–5%	0–3%	1–5%	1–4%	1–5%	0–4%	2–6%
WTA–SD (0.1, 3)	0–2%	0–5%	0–3%	1–6%	1–3%	0–6%	0–3%	1–6%
WTA–SD (0.2, 1)	0–4%	0–5%	0–4%	2–6%	1–4%	1–4%	0–4%	2–6%
WTA–SD (0.3, 1)	1–5%	1–4%	0–4%	2–6%	0–3%	1–4%	0–5%	1–6%
Standard–SD (0.1, 0)	1–6%	0–3%	0–2%	1–7%	1–3%	0–4%	0–2%	2–4%
Standard–SD (0.1, 1)	0–4%	0–5%	0–2%	1–6%	1–4%	0–5%	1–2%	2–7%
Standard–SD (0.1, 2)	1–4%	1–5%	0–2%	1–7%	1–4%	0–5%	0–2%	1–6%
Standard–SD (0.1, 3)	1–5%	1–5%	0–3%	1–7%	1–3%	1–4%	0–4%	2–5%
Standard–SD (0.2, 1)	1–4%	0–4%	0–2%	2–6%	0–2%	0–4%	0–3%	1–5%
Standard–SD (0.3, 1)	2–4%	1–4%	0–2%	2–6%	0–3%	0–5%	0–3%	1–6%

for jets of $R = 0.2$ and 0.4 in 20-GeV/c-wide $p_{\text{T}}^{\text{ch jet}}$ intervals in the 20–100 GeV/c range. Here, $N_{\text{jets}}(p_{\text{T}}^{\text{ch jet}})$ is the number of inclusive jets in a given $p_{\text{T}}^{\text{ch jet}}$ interval. In the groomed cases, the normalization factor N_{jets} is obtained by including the number of untagged jets (i.e. without any splitting in the jet that satisfies the SD condition, so that the grooming process fails) in the unfolding procedure. Therefore, the number of jets appearing in the ΔR_{axis} distributions differs from N_{jets} by the number of jets that are untagged.

Sections 5.1 and 5.2 present the experimental results as well as comparisons to predictions from MC generators and analytical calculations, respectively.

5.1 Comparison to MC generators

Figure 2 compares the measured Standard–SD distributions with predictions from Monte Carlo event generators, for jets of $R = 0.4$ (top) and 0.2 (bottom) in $40 < p_{\text{T}}^{\text{ch jet}} < 60$ GeV/c. Results for different $p_{\text{T}}^{\text{ch jet}}$ intervals are presented in Appendix A. The vertical error bars are statistical uncertainties, and the rectangles indicate the total systematic uncertainties. The solid (dashed) lines show results from PYTHIA 8 (Herwig 7). The bottom two panels in these figures correspond to the ratios of data to PYTHIA 8 and Herwig 7 distributions. The left panel of Fig. 2 shows the case in which z_{cut} is fixed at 0.1 and β is varied from 0 to 3. In the right panel, β is fixed at 1 and z_{cut} is varied from 0.1 to 0.3. These spectra are plotted with a logarithmic y-axis to better exhibit the entire distribution. Figure 3 shows the equivalent comparison for the case of the WTA–Standard and WTA–SD distributions.

Overall, the Standard–SD distributions are narrow and peaked at very small values. This implies that the Standard and SD axes are aligned and grooming does not significantly impact the jet direction. However, as the grooming becomes more aggressive (i.e. higher z_{cut} or smaller β), the alignment between the Standard and SD axes worsens somewhat. This trend is present for both $R = 0.2$ and $R = 0.4$. There is a maximum at $\Delta R_{\text{axis}}^{\text{Standard–SD}} = 0$ that corresponds to jets for which the first splitting after reclustering the jet with the C/A algorithm already satisfies the SD condition. As a result, the difference with respect to the Standard axis is exactly 0.

The shape of the $\Delta R_{\text{axis}}^{\text{Standard–SD}}$ spectra is better described by Herwig 7 than by PYTHIA 8. In the

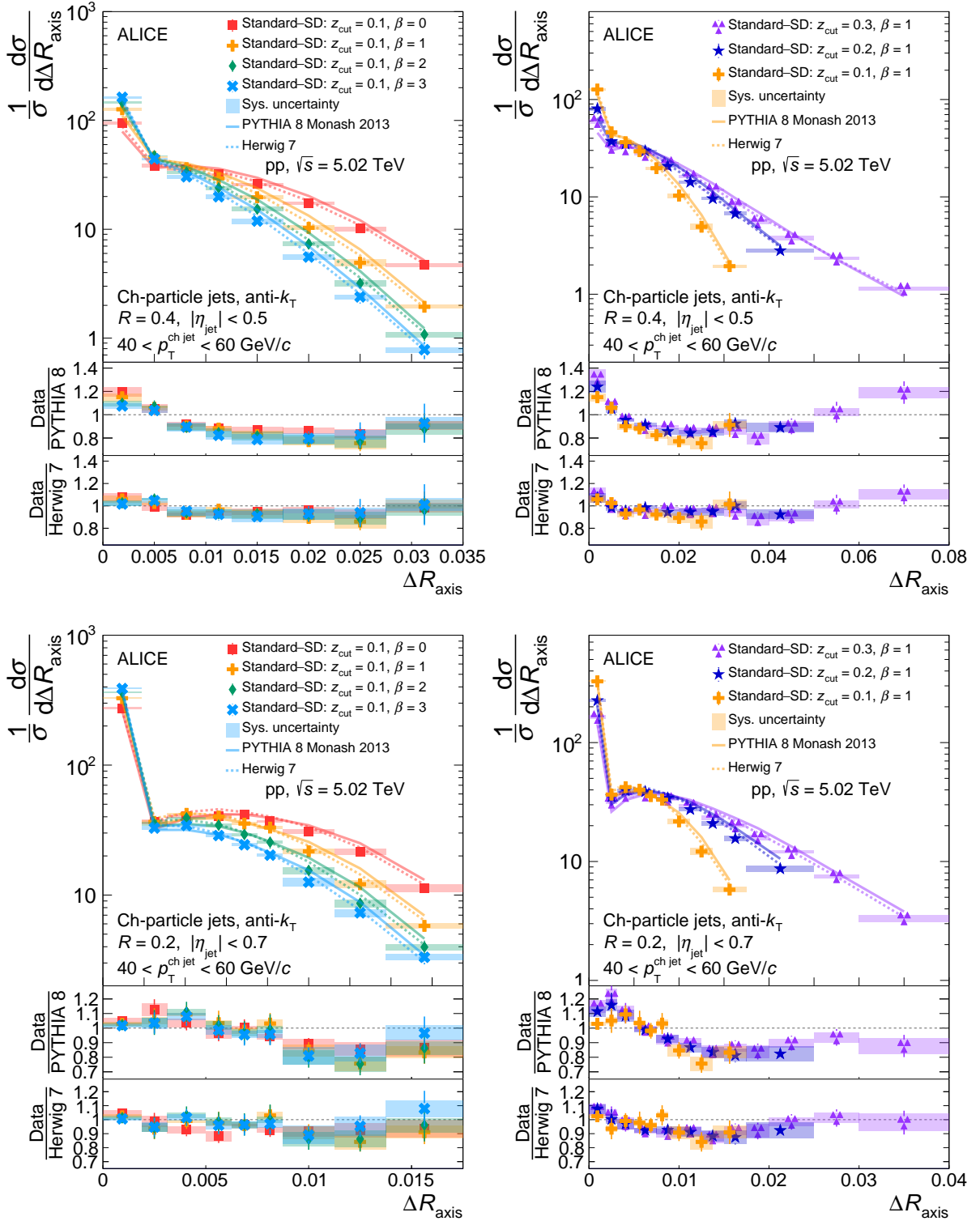


Figure 2: Comparison between the ΔR_{axis} Standard-SD measured distributions and Monte Carlo event generators for jets of $R = 0.4$ (top) and 0.2 (bottom) in $40 < p_{\text{T}}^{\text{ch jet}} < 60$ GeV/c. Left: distributions with $z_{\text{cut}} = 0.1$ and varying β . Right: distributions with $\beta = 1$ and varying z_{cut} .

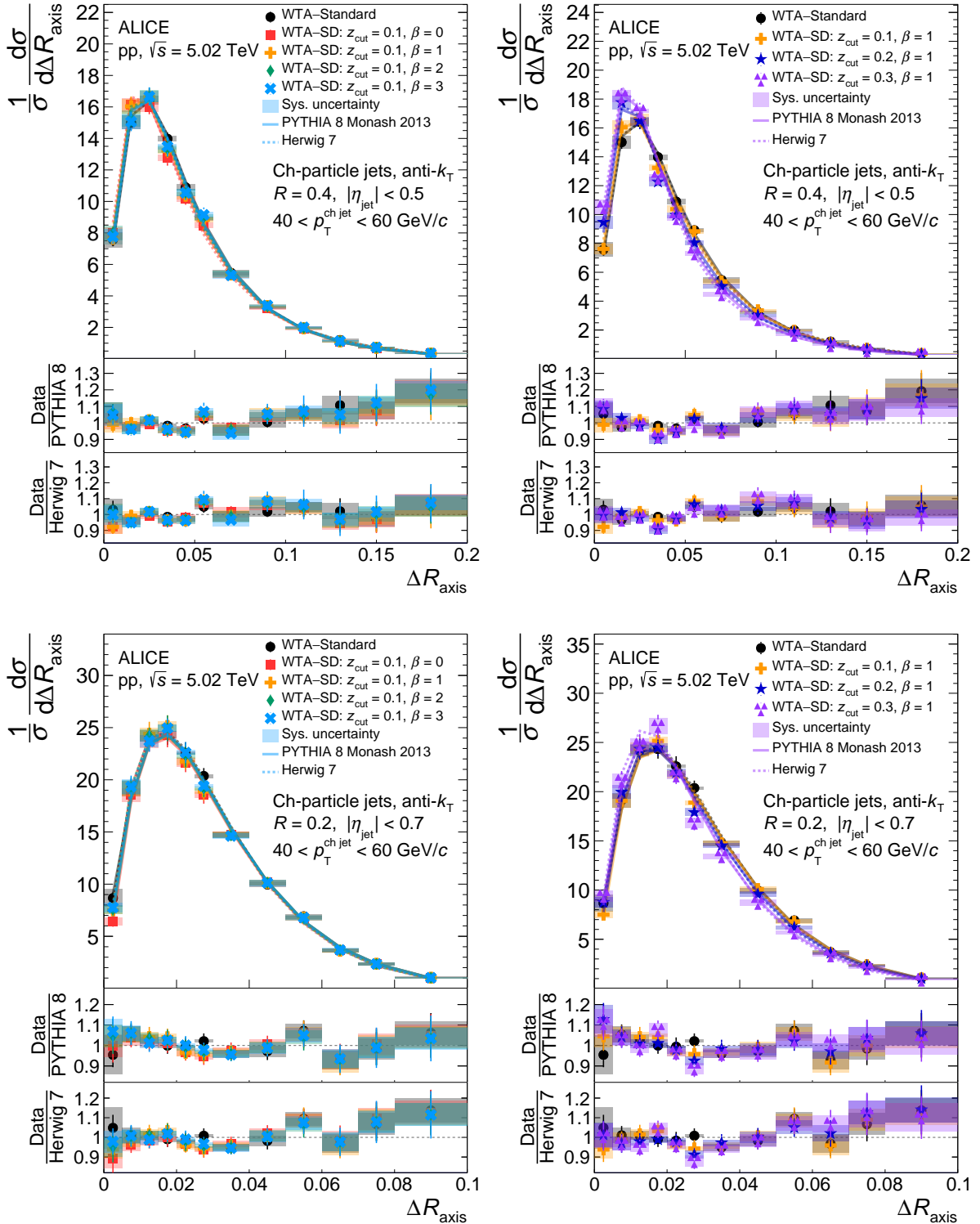


Figure 3: Comparison between the ΔR_{axis} WTA-Standard and WTA-SD measured distributions and Monte Carlo event generators for jets of $R = 0.4$ (top) and 0.2 (bottom) in $40 < p_T^{\text{ch jet}} < 60$ GeV/c. Left: distributions with $z_{\text{cut}} = 0.1$ and varying β . Right: distributions with $\beta = 1$ and varying z_{cut} .

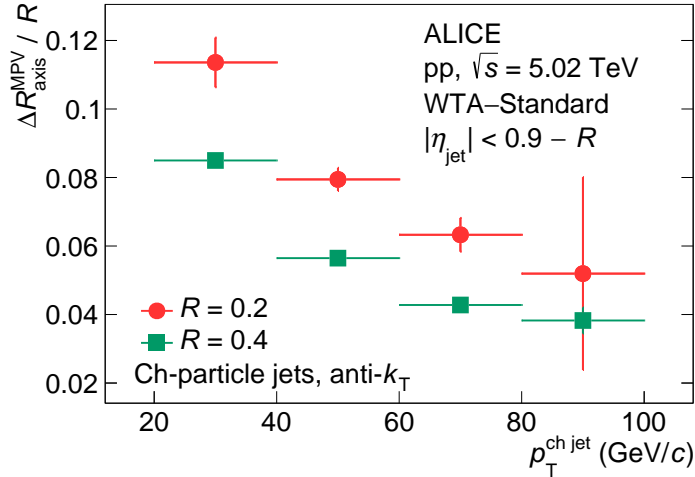


Figure 4: Distribution of the most-probable value of the WTA-Standard spectra as a function of $p_T^{\text{ch jet}}$ for $R = 0.2$ and $R = 0.4$.

$40 < p_T^{\text{ch jet}} < 60$ GeV/c range, bin-by-bin deviations with respect to PYTHIA 8 (Herwig 7) reach values up to $\approx 24\%$ ($\approx 7\%$). Given that this observable is particularly sensitive to soft-radiation effects, our data can be used to further constrain the hadronization models in these generators.

The ΔR_{axis} distributions for the WTA-Standard and WTA-SD cases are broader ($0 < \Delta R_{\text{axis}} \lesssim R/2$) and peak at larger ΔR_{axis} , showing substantial deviation between the WTA and Standard/SD jet axes. Additionally, these distributions show very low sensitivity to the parameters chosen in the Soft Drop grooming procedure.

The $\Delta R_{\text{axis}}^{\text{WTA-Standard}}$ and $\Delta R_{\text{axis}}^{\text{WTA-SD}}$ predictions from PYTHIA 8 and Herwig 7 generally agree with the data, deviating by up to $\approx 10\%$ in the $40 < p_T^{\text{ch jet}} < 60$ GeV/c interval and up to $\approx 40\%$ in several other $p_T^{\text{ch jet}}$ intervals. The largest deviations are at low values of ΔR_{axis} , corresponding to the region in which non-perturbative effects are significant. It should be noted, though, that the normalization convention implies that conclusions can only be made about the overall shape and not about a discrepancy in a specific ΔR_{axis} interval.

The axis differences with respect to WTA shift to lower ΔR_{axis} values at higher $p_T^{\text{ch jet}}$, implying that the WTA and Standard or SD axes are more aligned in more energetic jets. This is summarized in Fig. 4, where the most-probable value (MPV) of the $\Delta R_{\text{axis}}^{\text{WTA-Standard}}$ distribution normalized to the jet resolution parameter R is shown as a function of $p_T^{\text{ch jet}}$. The values in this figure are determined by repeatedly fitting a Landau distribution to the $\Delta R_{\text{axis}}^{\text{WTA-Standard}}$ spectra changing each time the fit range. A histogram is then filled with the peak-position values extracted from each fit. From this histogram, the mean and standard deviation are extracted as the central value and uncertainty, respectively. The values decrease from $\approx 11\%$ (8.5%) at low $p_T^{\text{ch jet}}$ to $\approx 5\%$ (4%) at high $p_T^{\text{ch jet}}$ for $R = 0.2$ (0.4).

5.2 Comparison to analytical calculations

The ΔR_{axis} observable has been calculated in the Soft Collinear Effective Theory (SCET) framework [67]. In this framework, the jet-production cross section is factorized into parton distribution functions (PDF), “hard”, and “jet” contributions in order to separate physics processes at different scales. The PDFs encode the probability of finding a parton with a given flavor and momentum fraction from a proton and are non-perturbative objects extracted from global fits to measured data (see, e.g. Refs. 68, 69). The SCET calculations presented here use the CT14 NLO PDF set [70]. The hard contribution encodes the short-distance physics, i.e. the hard scattering of one parton from each colliding proton, and the distribution of the resulting partons. Finally, the jet function describes the evolution of a final-state parton from the

hard scattering into a collimated jet. Large logarithms are resummed to Next-to-Leading Logarithmic (NLL) accuracy for the Standard-SD ΔR_{axis} , and NLL' for the WTA-Standard and WTA-SD ΔR_{axis} , including the contribution from non-global logarithms [71]. NLL' refers to the inclusion in the resummation of terms that formally only enter at Next-to-Next-to-Leading Logarithmic (NNLL) accuracy, but their inclusion in the NLL calculation improves the theoretical uncertainty. Specifically, logarithms of the grooming parameter z_{cut} and the observable ΔR_{axis} are resummed. Logarithms of the jet resolution parameter R are also resummed, which makes the calculations valid down to arbitrarily low values of R and allows for tests of such resummations. The resummed result is presented without matching to the fixed-order calculation in the high- ΔR_{axis} region.

Unlike other TMD-sensitive jet substructure observables, such as hadron-in-jet fragmentation [72, 73], ΔR_{axis} does not depend on collinear fragmentation functions. Thus, a significant source of uncertainty is removed from these calculations.

The leading hadronization correction for these observables includes terms of the form $\exp[-g_K(b_{\perp}; b_{\perp}^{\text{max}})]$ [35], where b_{\perp} is the Fourier conjugate of k_T , the projection of the transverse momentum of a jet axis transverse to the other axis in ΔR_{axis} . The function $g_K(b_{\perp}; b_{\perp}^{\text{max}})$ is the non-perturbative component of the Collins-Soper-Sterman (CSS) evolution kernel or rapidity anomalous dimension. In the so-called b_* prescription [74, 75] it is often parametrized as

$$g_K(b_{\perp}; b_{\perp}^{\text{max}}) = g_2(b_{\perp}^{\text{max}}) b_{\perp}^2. \quad (4)$$

In this work, the universality of the CSS kernel is tested by verifying that the ΔR_{axis} observables are well described across two resolution parameters R , and several grooming settings and $p_T^{\text{ch jet}}$ intervals with the same parameters in $g_K(b_{\perp}; b_{\perp}^{\text{max}})$ corresponding to $b_{\perp}^{\text{max}} = 1.5 (\text{GeV}/c)^{-1}$ and $g_2(b_{\perp}^{\text{max}}) = 0.18$ from a global data analysis to Drell-Yan lepton pair and Z^0 -boson production [76].

The analytic predictions are provided by the authors of Ref. 35 for the kinematics of our measurement at hadron level (i.e. after hadronization, in contrast to parton level) for full jets (i.e. including both charged and neutral hadrons), and without including multi-parton interaction (MPI) effects. To do a comparison to the measured distributions, the analytic predictions are corrected using data from Monte Carlo event generators. Final-state particles from pp events are clustered into full and charged-particle jets following the same procedure as in the data analysis (i.e. using the anti- k_T algorithm with the E recombination scheme for a given R), and the resulting jets are required to satisfy $|\eta_{\text{jet}}| < 0.9 - R$ and $p_T^{\text{jet}} > 5 \text{ GeV}/c$. The full and charged-particle jets are then geometrically matched following the matching procedure of the RM from the data analysis. This sample is used to construct a 4D response matrix that maps the p_T^{jet} and ΔR_{axis} dependence from full- to charged-particle-jet levels for each observable.

The analytic predictions are provided as normalized densities $(1/\sigma_{\text{jet}})(d\sigma_{\text{jet}}/d\Delta R_{\text{axis}})$ for the ΔR_{axis} observable in different p_T^{jet} intervals (of 5 GeV/ c width) for the nominal case, as well as for the results obtained by systematically varying the scales that appear in the calculation to account for theoretical uncertainties [35]. The first step in the correction corresponds to multiplying the spectrum by the average value of the inclusive cross section in the considered p_T^{jet} interval to obtain the distribution for $d\sigma_{\text{jet}}/d\Delta R_{\text{axis}}$. The cross section used was calculated at Next-to-Leading Order (NLO) with resummation of logarithms of the jet radius at NLL [77]. The scaled distributions are stored in 2D histograms in p_T and ΔR_{axis} and multiplied by the 4D response matrices described in the previous paragraph to obtain the analytic predictions for charged-particle jets. Subsequently, the resulting 2D histograms are corrected to account for MPI effects by multiplying bin-by-bin by the ratio of the simulated distribution without and with MPI effects included. The result is projected onto the observable axis for a range in $p_T^{\text{ch jet}}$ equal to that of the measured distribution. The final theory prediction corresponds to the curve obtained from the nominal calculation. Additionally, the other results obtained from the systematic scale variations are equally corrected, and the envelope of all resulting distributions is taken as the theoretical uncertainty on

the calculations.

The use of a Monte Carlo event generator in these corrections introduces a model dependence, the significance of which is explored by applying the correction procedure with two different generators: PYTHIA 8 with the Monash 2013 tune [61] and Herwig 7 with the default tune [78].

Figure 5 shows a subset of the comparison between the measured distributions and the corrected analytic predictions. Equivalent comparisons for the rest of all available predictions are presented in Appendix B. The black markers correspond to the distributions determined from measured data. These distributions are identical to those in Fig. 3 up to a normalization factor defined below. The vertical error bars correspond to the statistical uncertainties, and the rectangles correspond to the total systematic uncertainties. The colored curves correspond to the SCET-based analytic predictions corrected for charge and MPI effects using two event generators (PYTHIA 8 and Herwig 7).

Differences between the SCET predictions corrected with either Monte Carlo event generator are very small. This is due to the fact that, since the input calculations are provided at hadron level, the most significant correction is done to the p_T scale of the jet, and this correction is well modeled by both generators. Thus, the resulting distributions are not significantly model dependent.

The analytic calculations are only expected to describe the measured distributions in the perturbative region. The predictions presented here become non-perturbative approximately at $\Delta R_{\text{axis}} \lesssim \Delta R_{\text{axis}}^{\text{NP}} = \Lambda/p_T^{\text{ch jet}}$ [35], where Λ corresponds to the scale at which the strong coupling constant becomes non-perturbative. The red vertical line in Fig. 5 corresponds to this value calculated using $\Lambda = 1$ GeV and $p_T^{\text{ch jet}} = \bar{p}_T^{\text{ch jet}}$, the average jet-transverse-momentum value in the interval. The $\bar{p}_T^{\text{ch jet}}$ value for a given $p_T^{\text{ch jet}}$ interval was determined by fitting the measured spectra with a power law and subsequently analytically calculating the mean value in the interval. The comparison is done by normalizing both the measured distributions and analytic predictions so that $\int_{\Delta R_{\text{axis}}^{\text{NP}}}^{R/2} d\Delta R_{\text{axis}} (d\sigma/d\Delta R_{\text{axis}}) = 1$. The ΔR_{axis} interval that contains the value $\Delta R_{\text{axis}}^{\text{NP}}$ is defined to belong to the non-perturbative region and excluded from the integral. In reality, there is no sharp boundary between the perturbative and non-perturbative regimes, but a continuous transition. This vertical line is therefore an indicative value defined for the sake of the comparison.

The Standard-SD variable is also IRC safe and therefore calculable in the SCET framework. However, these calculations are computationally expensive and the results are not available at the time of this article. These distributions are particularly sensitive to soft effects, and thus also to the hadronization corrections.

5.3 Discussion of analytic calculations

The analytic predictions describe the measured distributions in the perturbative regime within uncertainties for all variations of the observable (i.e. jet-resolution parameter, grooming setting and $p_T^{\text{ch jet}}$) considered in the analysis. The agreement is excellent (largest deviations observed are within 10 to 20% in the lower p_T bins, where the smaller systematic uncertainties allow us to draw more precise conclusions) given the low $p_T^{\text{ch jet}}$ values from this measurement. Additionally, even though the distributions are normalized to their integral in the perturbative region, significant agreement is also found in the non-perturbative region, where the calculations are most sensitive to the non-perturbative correction. This agreement persists independently of jet-resolution parameter, grooming setting, and $p_T^{\text{ch jet}}$. There are larger shape differences between the data and analytic predictions for larger R .

The agreement at lower ΔR_{axis} values is increasingly due to the inclusion of the non-perturbative correction from Eq. 4. The measured distributions are compatible with the universal behavior of the non-perturbative component of the CSS evolution kernel to the extent this hadronization correction is well modeled. This is the first time this has been verified in jet substructure observables. The measurements

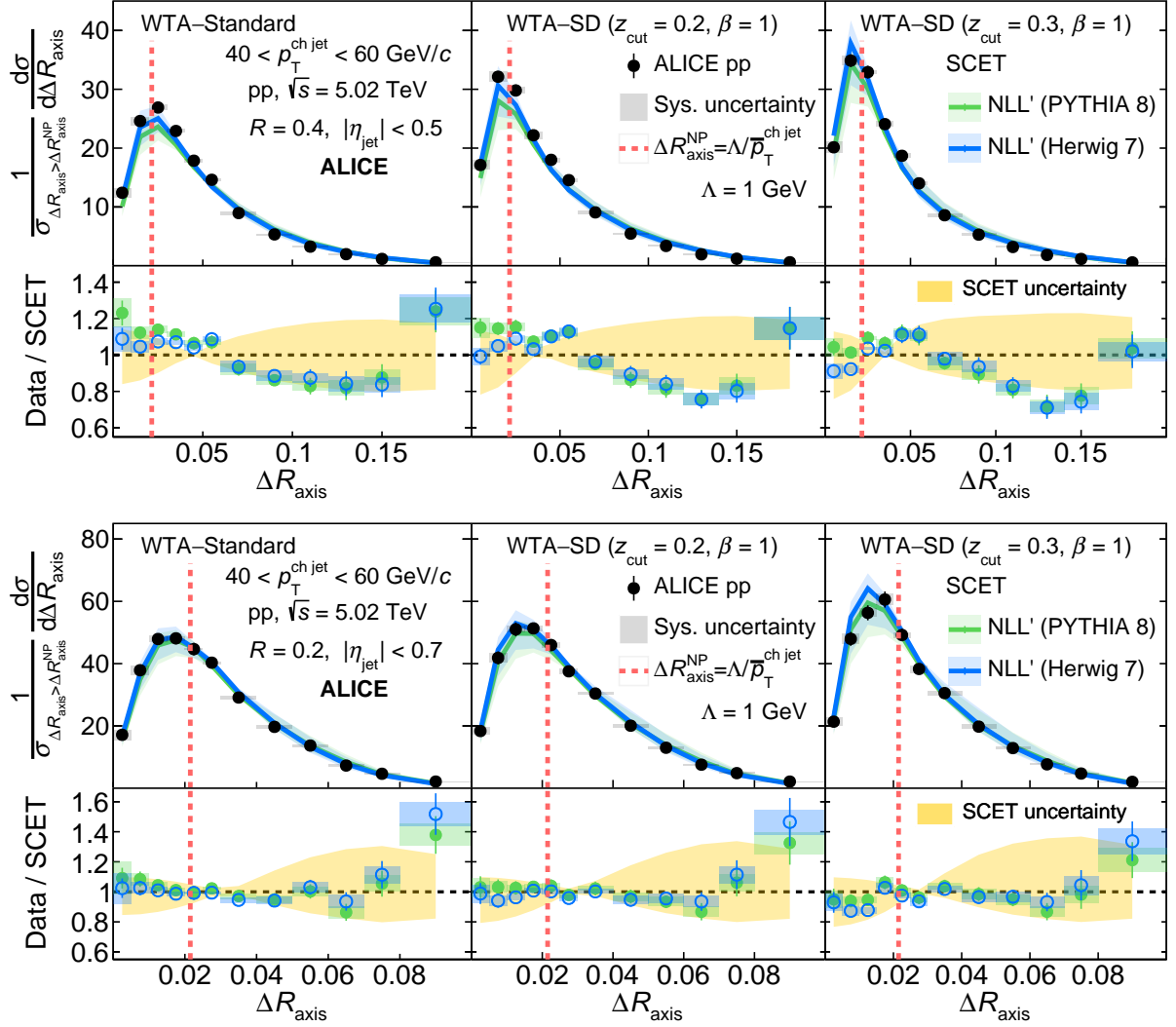


Figure 5: Comparison between measured distributions and analytic predictions for the difference between the WTA axis and the Standard (left), SD ($z_{\text{cut}} = 0.2, \beta = 1$) (center), and SD ($z_{\text{cut}} = 0.3, \beta = 1$) (right) axes for jets of $R = 0.4$ (top) and 0.2 (bottom) in the transverse momentum range $40 < p_T^{\text{ch,jet}} < 60$ GeV/c. The black markers correspond to the distributions determined from measured data. The vertical error bars correspond to the statistical uncertainties, and the rectangles correspond to the total systematic uncertainties. The colored curves correspond to the SCET-based analytic predictions corrected for charge and MPI effects using two event generators (PYTHIA 8 and Herwig 7). The vertical dashed line defines the approximate boundary between the non-perturbative and perturbative regions. Both the measured and analytic predictions are normalized so that the integral $\int_{\Delta R_{\text{axis}}^{\text{NP}}}^{R/2} d\Delta R_{\text{axis}} (d\sigma/d\Delta R_{\text{axis}}) = 1$. The bottom panels show the data/SCET ratios. The colored rectangles correspond to the systematic uncertainty of the measured distribution. The size of the theoretical uncertainty in the analytic predictions is shown as a yellow band.

presented in this article should be included in future global fits to further increase the precision of the experimental extractions of the non-perturbative component of the CSS kernel.

The theoretical uncertainties in the analytic predictions are significant, and reducing them can lead to a higher-precision test. Specifically, as shown in the ratio plots from Fig. 5, while the measured distributions and the calculations agree within uncertainties, there are systematic shape differences between them. For instance, there is a sudden rise in the interval at the highest ΔR_{axis} which can be related to the lack of matching to a fixed-order calculation or power corrections in the observable in the SCET prediction. However, because the distributions are self-normalized, the disagreement cannot be pinned to a specific ΔR_{axis} value.

6 Conclusions

The first measurement of the angle between the Standard, Soft Drop groomed, and Winner-Take-All charged-jet axes is reported. The measurement was carried out in pp collisions at $\sqrt{s} = 5.02$ TeV with the ALICE detector for jets of $R = 0.2$ and 0.4 . This analysis focused on jets below 100 GeV/ c , where non-perturbative effects are more important than in highly energetic jets. Jet grooming does not substantially change the jet axis direction. The WTA and Standard jet axes differ substantially, though, showing that the Standard jet axis does not generally point in the direction of the highest-momentum jet fragment. However, the WTA and Standard or SD axes become more aligned in more energetic jets. The motivation to use the WTA axis arises from its insensitivity to soft radiation; it is amenable to perturbative calculations and is expected to be less modified in the medium created in ultrarelativistic nucleus–nucleus collisions.

The distributions from PYTHIA 8 and Herwig 7 show overall good agreement with the data; both groomed and ungroomed jet axis differences with WTA are generally described within the uncertainties. The Standard–SD jet axis difference is better described by Herwig 7 than by PYTHIA 8, suggesting that Herwig better reproduces the soft splittings which are groomed away by Soft Drop. There is also good agreement between the analytic predictions and the measured spectra, even in the region of ΔR_{axis} where non-perturbative physics is important. Within the precision of the measurement and analytic calculations, our result is compatible with the universality of the non-perturbative component of the Collins–Soper–Sterman (CSS) TMD evolution kernel. This study constitutes the first experimental verification of such compatibility in the context of jet-substructure measurements.

These measurements shed light on the interplay between perturbative and non-perturbative effects. The majority of jets produced in pp collisions at this center-of-mass energy are initiated by gluons. It will be illuminating to compare these distributions to those from quark-initiated jets. This can be done by measuring ΔR_{axis} in, for example, heavy-flavor jets or photon–jet coincidences.

The angle between different jet axes may also reflect medium modification of jet angular substructure in heavy-ion collisions. The results presented here will provide a valuable baseline for Pb–Pb studies.

Acknowledgements

The ALICE Collaboration gratefully acknowledges Felix Ringer for providing theoretical predictions.

The ALICE Collaboration would like to thank all its engineers and technicians for their invaluable contributions to the construction of the experiment and the CERN accelerator teams for the outstanding performance of the LHC complex. The ALICE Collaboration gratefully acknowledges the resources and support provided by all Grid centres and the Worldwide LHC Computing Grid (WLCG) collaboration. The ALICE Collaboration acknowledges the following funding agencies for their support in building and running the ALICE detector: A. I. Alikhanyan National Science Laboratory (Yerevan Physics Institute) Foundation (ANSL), State Committee of Science and World Federation of Scientists (WFS), Armenia; Austrian Academy of Sciences, Austrian Science Fund (FWF): [M 2467-N36] and Nationalstiftung für Forschung, Technologie und Entwicklung, Austria; Ministry of Communications and High Technologies, National Nuclear Research Center, Azerbaijan; Conselho Nacional de Desenvolvimento Científico e Tecnológico (CNPq), Financiadora de Estudos e Projetos (Finep), Fundação de Amparo à Pesquisa do Estado de São Paulo (FAPESP) and Universidade Federal do Rio Grande do Sul (UFRGS), Brazil; Bulgarian Ministry of Education and Science, within the National Roadmap for Research Infrastructures 2020-2027 (object CERN), Bulgaria; Ministry of Education of China (MOEC), Ministry of Science & Technology of China (MSTC) and National Natural Science Foundation of China (NSFC), China; Ministry of Science and Education and Croatian Science Foundation, Croatia; Centro de Aplicaciones Tecnológicas y Desarrollo Nuclear (CEADEN), Cubaenergía, Cuba; Ministry of Education, Youth and Sports of the Czech Republic, Czech Republic; The Danish Council for Independent Research | Natural Sciences, the VILLUM FONDEN and Danish National Research Foundation (DNRF), Denmark; Helsinki Institute of Physics (HIP), Finland; Commissariat à l’Energie Atomique (CEA) and Institut National de Physique Nucléaire et de Physique des Particules (IN2P3) and Centre National de la Recherche Scientifique (CNRS), France; Bundesministerium für Bildung und Forschung (BMBF) and GSI Helmholtzzentrum für Schwerionenforschung GmbH, Germany; General Secretariat for Research and Technology, Ministry of Education, Research and Religions, Greece; National Research, Development and Innovation Office, Hungary; Department of Atomic Energy Government of India (DAE), Department of Science and Technology, Government of India (DST), University Grants Commission, Government of India (UGC) and Council of Scientific and Industrial Research (CSIR), India; National Research and Innovation Agency - BRIN, Indonesia; Istituto Nazionale di Fisica Nucleare (INFN), Italy; Japanese Ministry of Education, Culture, Sports, Science and Technology (MEXT) and Japan Society for the Promotion of Science (JSPS) KAKENHI, Japan; Consejo Nacional de Ciencia (CONACYT) y Tecnología, through Fondo de Cooperación Internacional en Ciencia y Tecnología (FONCICYT) and Dirección General de Asuntos del Personal Académico (DGAPA), Mexico; Nederlandse Organisatie voor Wetenschappelijk Onderzoek (NWO), Netherlands; The Research Council of Norway, Norway; Commission on Science and Technology for Sustainable Development in the South (COMSATS), Pakistan; Pontificia Universidad Católica del Perú, Peru; Ministry of Education and Science, National Science Centre and WUT ID-UB, Poland; Korea Institute of Science and Technology Information and National Research Foundation of Korea (NRF), Republic of Korea; Ministry of Education and Scientific Research, Institute of Atomic Physics, Ministry of Research and Innovation and Institute of Atomic Physics and University Politehnica of Bucharest, Romania; Ministry of Education, Science, Research and Sport of the Slovak Republic, Slovakia; National Research Foundation of South Africa, South Africa; Swedish Research Council (VR) and Knut & Alice Wallenberg Foundation (KAW), Sweden; European Organization for Nuclear Research, Switzerland; Suranaree University of Technology (SUT), National Science and Technology Development Agency (NSTDA), Thailand Science Research and Innovation (TSRI) and National Science, Research and Innovation Fund (NSRF), Thailand; Turkish Energy, Nuclear and Mineral Research Agency (TENMAK), Turkey; National Academy of Sciences of Ukraine, Ukraine; Science and Technology Facilities Council (STFC), United Kingdom; National Science Foundation of the United States of America (NSF) and United States Department of Energy, Office of Nuclear Physics

(DOE NP), United States of America. In addition, individual groups or members have received support from: Marie Skłodowska Curie, European Research Council, Strong 2020 - Horizon 2020 (grant nos. 950692, 824093, 896850), European Union; Academy of Finland (Center of Excellence in Quark Matter) (grant nos. 346327, 346328), Finland; Programa de Apoyos para la Superación del Personal Académico, UNAM, Mexico.

References

- [1] R. Kogler *et al.*, “Jet Substructure at the Large Hadron Collider: Experimental Review”, *Rev. Mod. Phys.* **91** (2019) 045003, arXiv:1803.06991 [hep-ex].
- [2] A. J. Larkoski, I. Moulton, and B. Nachman, “Jet Substructure at the Large Hadron Collider: A Review of Recent Advances in Theory and Machine Learning”, *Phys. Rept.* **841** (2020) 1–63, arXiv:1709.04464 [hep-ph].
- [3] S. Marzani, G. Soyez, and M. Spannowsky, *Looking inside jets: an introduction to jet substructure and boosted-object phenomenology*, vol. 958. Springer, (2019). arXiv:1901.10342 [hep-ph].
- [4] ALICE Collaboration, B. B. Abelev *et al.*, “Charged jet cross sections and properties in proton-proton collisions at $\sqrt{s} = 7$ TeV”, *Phys. Rev. D* **91** (2015) 112012, arXiv:1411.4969 [nucl-ex].
- [5] ALICE Collaboration, S. Acharya *et al.*, “Jet fragmentation transverse momentum measurements from di-hadron correlations in $\sqrt{s} = 7$ TeV pp and $\sqrt{s_{NN}} = 5.02$ TeV p–Pb collisions”, *JHEP* **03** (2019) 169, arXiv:1811.09742 [nucl-ex].
- [6] ALICE Collaboration, S. Acharya *et al.*, “Charged jet cross section and fragmentation in proton-proton collisions at $\sqrt{s} = 7$ TeV”, *Phys. Rev. D* **99** (2019) 012016, arXiv:1809.03232 [nucl-ex].
- [7] ALICE Collaboration, S. Acharya *et al.*, “Measurement of the production of charm jets tagged with D^0 mesons in pp collisions at $\sqrt{s} = 7$ TeV”, *JHEP* **08** (2019) 133, arXiv:1905.02510 [nucl-ex].
- [8] ALICE Collaboration, S. Acharya *et al.*, “Exploration of jet substructure using iterative declustering in pp and Pb–Pb collisions at LHC energies”, *Phys. Lett. B* **802** (2020) 135227, arXiv:1905.02512 [nucl-ex].
- [9] ALICE Collaboration, S. Acharya *et al.*, “Measurements of the groomed and ungroomed jet angularities in pp collisions at $\sqrt{s} = 5.02$ TeV”, *JHEP* **05** (2022) 061, arXiv:2107.11303 [nucl-ex].
- [10] **A Large Ion Collider Experiment**, ALICE Collaboration, S. Acharya *et al.*, “Measurement of the groomed jet radius and momentum splitting fraction in pp and Pb–Pb collisions at $\sqrt{s_{NN}} = 5.02$ TeV”, *Phys. Rev. Lett.* **128** (2022) 102001, arXiv:2107.12984 [nucl-ex].
- [11] ALICE Collaboration, S. Acharya *et al.*, “First measurements of N-subjettiness in central Pb–Pb collisions at $\sqrt{s_{NN}} = 2.76$ TeV”, *JHEP* **10** (2021) 003, arXiv:2105.04936 [nucl-ex].
- [12] ALICE Collaboration, S. Acharya *et al.*, “Direct observation of the dead-cone effect in quantum chromodynamics”, *Nature* **605** (2022) 440–446, arXiv:2106.05713 [nucl-ex]. [Erratum: *Nature* 607, E22 (2022)].
- [13] ATLAS Collaboration, G. Aad *et al.*, “Jet mass and substructure of inclusive jets in $\sqrt{s} = 7$ TeV pp collisions with the ATLAS experiment”, *JHEP* **05** (2012) 128, arXiv:1203.4606 [hep-ex].

- [14] **ATLAS** Collaboration, G. Aad *et al.*, “ATLAS Measurements of the Properties of Jets for Boosted Particle Searches”, *Phys. Rev. D* **86** (2012) 072006, arXiv:1206.5369 [hep-ex].
- [15] **ATLAS** Collaboration, G. Aad *et al.*, “Measurement of jet shapes in top-quark pair events at $\sqrt{s} = 7$ TeV using the ATLAS detector”, *Eur. Phys. J. C* **73** (2013) 2676, arXiv:1307.5749 [hep-ex].
- [16] **ATLAS** Collaboration, M. Aaboud *et al.*, “Measurement of the Soft-Drop Jet Mass in pp Collisions at $\sqrt{s} = 13$ TeV with the ATLAS Detector”, *Phys. Rev. Lett.* **121** (2018) 092001, arXiv:1711.08341 [hep-ex].
- [17] **ATLAS** Collaboration, M. Aaboud *et al.*, “Measurement of jet-substructure observables in top quark, W boson and light jet production in proton-proton collisions at $\sqrt{s} = 13$ TeV with the ATLAS detector”, *JHEP* **08** (2019) 033, arXiv:1903.02942 [hep-ex].
- [18] **ATLAS** Collaboration, G. Aad *et al.*, “Properties of jet fragmentation using charged particles measured with the ATLAS detector in pp collisions at $\sqrt{s} = 13$ TeV”, *Phys. Rev. D* **100** (2019) 052011, arXiv:1906.09254 [hep-ex].
- [19] **ATLAS** Collaboration, G. Aad *et al.*, “Measurement of soft-drop jet observables in pp collisions with the ATLAS detector at $\sqrt{s} = 13$ TeV”, *Phys. Rev. D* **101** (2020) 052007, arXiv:1912.09837 [hep-ex].
- [20] **ATLAS** Collaboration, G. Aad *et al.*, “Measurement of the Lund Jet Plane Using Charged Particles in 13 TeV Proton-Proton Collisions with the ATLAS Detector”, *Phys. Rev. Lett.* **124** (2020) 222002, arXiv:2004.03540 [hep-ex].
- [21] **ATLAS** Collaboration, G. Aad *et al.*, “Measurement of the jet mass in high transverse momentum $Z(\rightarrow b\bar{b})\gamma$ production at $\sqrt{s} = 13$ TeV using the ATLAS detector”, *Phys. Lett. B* **812** (Jan, 2021) 135991, arXiv:1907.07093 [hep-ex].
- [22] **CMS** Collaboration, S. Chatrchyan *et al.*, “Shape, Transverse Size, and Charged Hadron Multiplicity of Jets in pp Collisions at 7 TeV”, *JHEP* **06** (2012) 160, arXiv:1204.3170 [hep-ex].
- [23] **CMS** Collaboration, S. Chatrchyan *et al.*, “Measurement of jet fragmentation into charged particles in pp and PbPb collisions at $\sqrt{s_{NN}} = 2.76$ TeV”, *JHEP* **10** (2012) 087, arXiv:1205.5872 [nucl-ex].
- [24] **CMS** Collaboration, S. Chatrchyan *et al.*, “Measurement of Jet Fragmentation in PbPb and pp Collisions at $\sqrt{s_{NN}} = 2.76$ TeV”, *Phys. Rev. C* **90** (2014) 024908, arXiv:1406.0932 [nucl-ex].
- [25] **CMS** Collaboration, A. M. Sirunyan *et al.*, “Measurements of jet charge with dijet events in pp collisions at $\sqrt{s} = 8$ TeV”, *JHEP* **10** (2017) 131, arXiv:1706.05868 [hep-ex].
- [26] **CMS** Collaboration, A. M. Sirunyan *et al.*, “Measurement of the Splitting Function in pp and Pb-Pb Collisions at $\sqrt{s_{NN}} = 5.02$ TeV”, *Phys. Rev. Lett.* **120** (2018) 142302, arXiv:1708.09429 [nucl-ex].
- [27] **CMS** Collaboration, A. M. Sirunyan *et al.*, “Measurements of the differential jet cross section as a function of the jet mass in dijet events from proton-proton collisions at $\sqrt{s} = 13$ TeV”, *JHEP* **11** (2018) 113, arXiv:1807.05974 [hep-ex].
- [28] **CMS** Collaboration, A. M. Sirunyan *et al.*, “Jet Shapes of Isolated Photon-Tagged Jets in Pb-Pb and pp Collisions at $\sqrt{s_{NN}} = 5.02$ TeV”, *Phys. Rev. Lett.* **122** (2019) 152001, arXiv:1809.08602 [hep-ex].

- [29] **CMS** Collaboration, A. Tumasyan *et al.*, “Study of quark and gluon jet substructure in Z+jet and dijet events from pp collisions”, *JHEP* **01** (2022) 188, arXiv:2109.03340 [hep-ex].
- [30] **LHCb** Collaboration, R. Aaij *et al.*, “Study of J/ψ Production in Jets”, *Phys. Rev. Lett.* **118** (2017) 192001, arXiv:1701.05116 [hep-ex].
- [31] **LHCb** Collaboration, R. Aaij *et al.*, “Measurement of charged hadron production in Z-tagged jets in proton-proton collisions at $\sqrt{s} = 8$ TeV”, *Phys. Rev. Lett.* **123** (2019) 232001, arXiv:1904.08878 [hep-ex].
- [32] **STAR** Collaboration, J. Adam *et al.*, “Measurement of groomed jet substructure observables in p+p collisions at $\sqrt{s} = 200$ GeV with STAR”, *Phys. Lett. B* **811** (2020) 135846, arXiv:2003.02114 [hep-ex].
- [33] **STAR** Collaboration, M. Abdallah *et al.*, “Invariant Jet Mass Measurements in pp Collisions at $\sqrt{s} = 200$ GeV at RHIC”, *Phys. Rev. D* **104** (2021) 052007, arXiv:2103.13286 [hep-ex].
- [34] **STAR** Collaboration, M. S. Abdallah *et al.*, “Differential measurements of jet substructure and partonic energy loss in Au+Au collisions at $\sqrt{S_{NN}} = 200$ GeV”, *Phys. Rev. C* **105** (2022) 044906, arXiv:2109.09793 [nucl-ex].
- [35] P. Cal, D. Neill, F. Ringer, and W. J. Waalewijn, “Calculating the angle between jet axes”, *JHEP* **04** (2020) 211, arXiv:1911.06840 [hep-ph].
- [36] M. Cacciari, G. P. Salam, and G. Soyez, “The anti- k_t jet clustering algorithm”, *JHEP* **04** (2008) 063, arXiv:0802.1189 [hep-ph].
- [37] Y. L. Dokshitzer, G. D. Leder, S. Moretti, and B. R. Webber, “Better jet clustering algorithms”, *JHEP* **08** (1997) 001, arXiv:hep-ph/9707323.
- [38] M. Wobisch and T. Wengler, “Hadronization corrections to jet cross-sections in deep inelastic scattering”, in *Workshop on Monte Carlo Generators for HERA Physics (Plenary Starting Meeting)*, pp. 270–279. 4, 1998. arXiv:hep-ph/9907280.
- [39] D. Bertolini, T. Chan, and J. Thaler, “Jet Observables Without Jet Algorithms”, *JHEP* **04** (2014) 013, arXiv:1310.7584 [hep-ph].
- [40] A. A. Vladimirov, “Self-contained definition of the Collins–Soper kernel”, *Phys. Rev. Lett.* **125** (2020) 192002, arXiv:2003.02288 [hep-ph].
- [41] F. Landry, R. Brock, P. M. Nadolsky, and C. P. Yuan, “Tevatron Run-1 Z boson data and Collins–Soper–Sterman resummation formalism”, *Phys. Rev. D* **67** (2003) 073016, arXiv:hep-ph/0212159.
- [42] P. Sun, J. Isaacson, C. P. Yuan, and F. Yuan, “Nonperturbative functions for SIDIS and Drell–Yan processes”, *Int. J. Mod. Phys. A* **33** (2018) 1841006, arXiv:1406.3073 [hep-ph].
- [43] A. Bacchetta, F. Delcarro, C. Pisano, M. Radici, and A. Signori, “Extraction of partonic transverse momentum distributions from semi-inclusive deep-inelastic scattering, Drell–Yan and Z-boson production”, *JHEP* **06** (2017) 081, arXiv:1703.10157 [hep-ph]. [Erratum: *JHEP* **06**, 051 (2019)].
- [44] V. Bertone, I. Scimemi, and A. Vladimirov, “Extraction of unpolarized quark transverse momentum dependent parton distributions from Drell–Yan/Z-boson production”, *JHEP* **06** (2019) 028, arXiv:1902.08474 [hep-ph].

- [45] M. A. Ebert, I. W. Stewart, and Y. Zhao, “Determining the Nonperturbative Collins–Soper Kernel From Lattice QCD”, *Phys. Rev. D* **99** (2019) 034505, arXiv:1811.00026 [hep-ph].
- [46] P. Shanahan, M. Wagman, and Y. Zhao, “Collins–Soper kernel for TMD evolution from lattice QCD”, *Phys. Rev. D* **102** (2020) 014511, arXiv:2003.06063 [hep-lat].
- [47] B. V. Jacak and B. Müller, “The exploration of hot nuclear matter”, *Science* **337** (Jul, 2012) 310–314.
- [48] W. Busza, K. Rajagopal, and W. van der Schee, “Heavy Ion Collisions: The Big Picture, and the Big Questions”, *Ann. Rev. Nucl. Part. Sci.* **68** (2018) 339–376, arXiv:1802.04801 [hep-ph].
- [49] A. J. Larkoski, S. Marzani, G. Soyez, and J. Thaler, “Soft Drop”, *JHEP* **05** (2014) 146, arXiv:1402.2657 [hep-ph].
- [50] L. Evans (ed.) and P. Bryant (ed.), “LHC Machine”, *JINST* **3** (2008) S08001.
- [51] ALICE Collaboration, B. B. Abelev *et al.*, “Performance of the ALICE Experiment at the CERN LHC”, *Int. J. Mod. Phys. A* **29** (2014) 1430044, arXiv:1402.4476 [nucl-ex].
- [52] ALICE Collaboration, K. Aamodt *et al.*, “The ALICE experiment at the CERN LHC”, *JINST* **3** (2008) S08002.
- [53] ALICE Collaboration, E. Abbas *et al.*, “Performance of the ALICE VZERO system”, *JINST* **8** (2013) P10016, arXiv:1306.3130 [nucl-ex].
- [54] ALICE Collaboration, S. Acharya *et al.*, “Measurements of inclusive jet spectra in pp and central Pb–Pb collisions at $\sqrt{s_{NN}} = 5.02$ TeV”, *Phys. Rev. C* **101** (2020) 034911, arXiv:1909.09718 [nucl-ex].
- [55] ALICE Collaboration, S. Acharya *et al.*, “ALICE 2017 luminosity determination for pp collisions at $\sqrt{s} = 5$ TeV”, ALICE-PUBLIC-2018-014. <https://cds.cern.ch/record/2648933>.
- [56] ALICE Collaboration, K. Aamodt *et al.*, “Alignment of the ALICE Inner Tracking System with cosmic-ray tracks”, *JINST* **5** (2010) P03003, arXiv:1001.0502 [physics.ins-det].
- [57] J. Alme *et al.*, “The ALICE TPC, a large 3-dimensional tracking device with fast readout for ultra-high multiplicity events”, *Nucl. Instrum. Meth. A* **622** (2010) 316–367, arXiv:1001.1950 [physics.ins-det].
- [58] ALICE Collaboration, S. Acharya *et al.*, “Measurement of charged jet cross section in pp collisions at $\sqrt{s} = 5.02$ TeV”, *Phys. Rev. D* **100** (2019) 092004, arXiv:1905.02536 [nucl-ex].
- [59] M. Cacciari, G. P. Salam, and G. Soyez, “FastJet User Manual”, *Eur. Phys. J. C* **72** (2012) 1896, arXiv:1111.6097 [hep-ph].
- [60] T. Sjöstrand *et al.*, “An introduction to PYTHIA 8.2”, *Comput. Phys. Commun.* **191** (2015) 159–177, arXiv:1410.3012 [hep-ph].
- [61] P. Skands, S. Carrazza, and J. Rojo, “Tuning PYTHIA 8.1: the Monash 2013 Tune”, *Eur. Phys. J. C* **74** (2014) 3024, arXiv:1404.5630 [hep-ph].
- [62] R. Brun, F. Bruyant, M. Maire, A. C. McPherson, and P. Zancarini, *GEANT 3: user’s guide Geant 3.10, Geant 3.11; rev. version*. CERN, Geneva, Sep, 1987. <https://cds.cern.ch/record/1119728>.

- [63] ALICE Collaboration, “The ALICE definition of primary particles”,
<https://cds.cern.ch/record/2270008>.
- [64] G. D’Agostini, “A multidimensional unfolding method based on Bayes’ theorem”, *Nucl. Instrum. Meth. A* **362** (1994) 487 – 498.
- [65] G. D’Agostini, “Improved iterative Bayesian unfolding”, in *Alliance Workshop on Unfolding and Data Correction*. 10, 2010. arXiv:1010.0632 [physics.data-an].
- [66] <https://hepunix.rl.ac.uk/~adye/software/unfold/RooUnfold.html>.
- [67] C. W. Bauer, D. Pirjol, and I. W. Stewart, “Soft collinear factorization in effective field theory”, *Phys. Rev. D* **65** (2002) 054022, arXiv:hep-ph/0109045.
- [68] H.-L. Lai *et al.*, “New parton distributions for collider physics”, *Phys. Rev. D* **82** (2010) 074024, arXiv:1007.2241 [hep-ph].
- [69] J. Gao *et al.*, “CT10 next-to-next-to-leading order global analysis of QCD”, *Phys. Rev. D* **89** (2014) 033009, arXiv:1302.6246 [hep-ph].
- [70] S. Dulat *et al.*, “New parton distribution functions from a global analysis of quantum chromodynamics”, *Phys. Rev. D* **93** (2016) 033006, arXiv:1506.07443 [hep-ph].
- [71] M. Dasgupta and G. P. Salam, “Resummation of nonglobal QCD observables”, *Phys. Lett. B* **512** (2001) 323–330, arXiv:hep-ph/0104277.
- [72] R. Bain, Y. Makris, and T. Mehen, “Transverse Momentum Dependent Fragmenting Jet Functions with Applications to Quarkonium Production”, *JHEP* **11** (2016) 144, arXiv:1610.06508 [hep-ph].
- [73] Z.-B. Kang, X. Liu, F. Ringer, and H. Xing, “The transverse momentum distribution of hadrons within jets”, *JHEP* **11** (2017) 068, arXiv:1705.08443 [hep-ph].
- [74] J. C. Collins, D. E. Soper, and G. F. Sterman, “Transverse Momentum Distribution in Drell-Yan Pair and W and Z Boson Production”, *Nucl. Phys. B* **250** (1985) 199–224.
- [75] Y. Makris, D. Neill, and V. Vaidya, “Probing Transverse-Momentum Dependent Evolution With Groomed Jets”, *JHEP* **07** (2018) 167, arXiv:1712.07653 [hep-ph].
- [76] A. V. Konychev and P. M. Nadolsky, “Universality of the Collins–Soper–Sterman nonperturbative function in gauge boson production”, *Phys. Lett. B* **633** (2006) 710–714, arXiv:hep-ph/0506225.
- [77] Z.-B. Kang, F. Ringer, and I. Vitev, “The semi-inclusive jet function in SCET and small radius resummation for inclusive jet production”, *JHEP* **10** (2016) 125, arXiv:1606.06732 [hep-ph].
- [78] S. Gieseke, C. Rohr, and A. Siodmok, “Colour reconnections in Herwig++”, *Eur. Phys. J. C* **72** (Nov, 2012) 2225, arXiv:1206.0041 [hep-ph].

A Comparison to Monte Carlo event generators

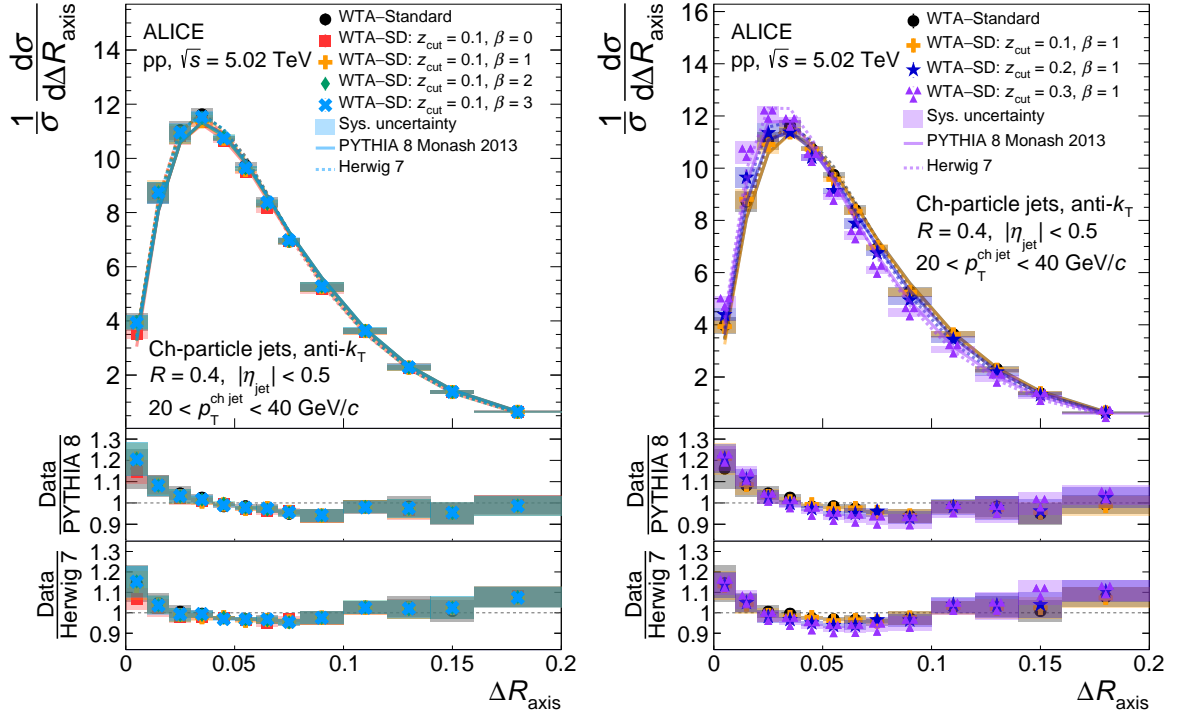


Figure A.1: Comparison between ΔR_{axis} WTA-Standard and WTA-SD measured distributions and Monte Carlo event generators for jets of $R = 0.4$ in $20 < p_T^{\text{jet}} < 40$ GeV/c. Left: distributions with $z_{\text{cut}} = 0.1$ and varying β . Right: distributions with $\beta = 1$ and varying z_{cut} .

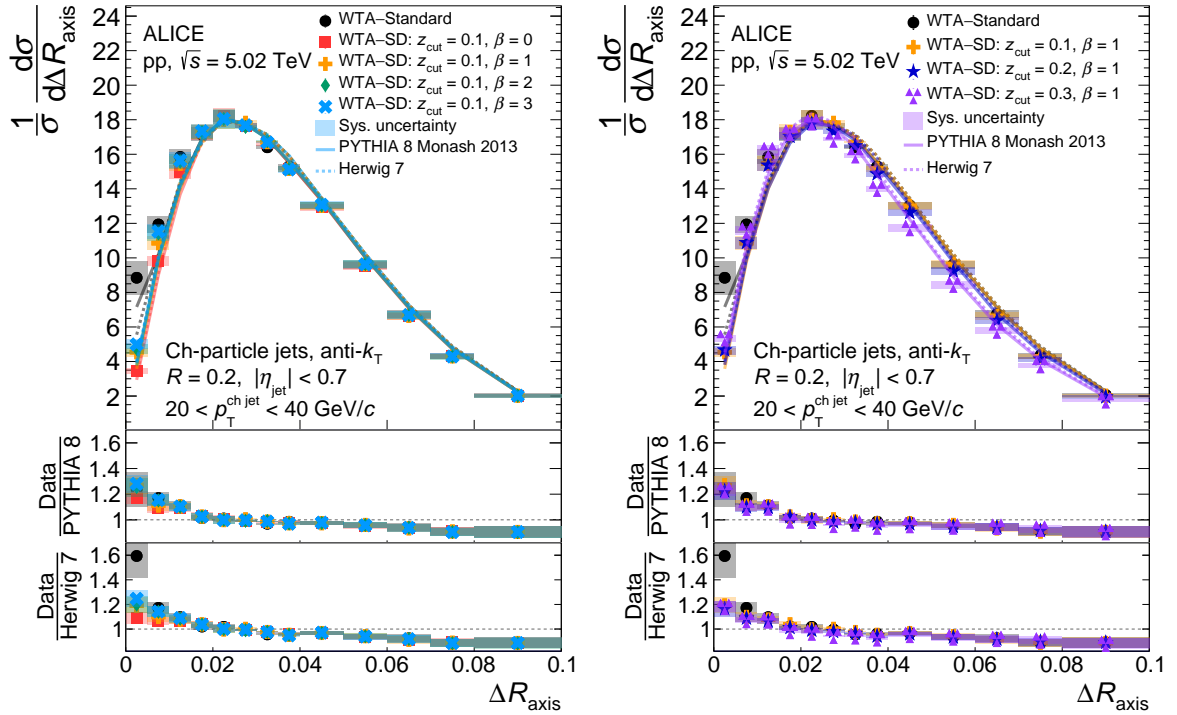


Figure A.2: Same as Figure A.1 for $R = 0.2$.

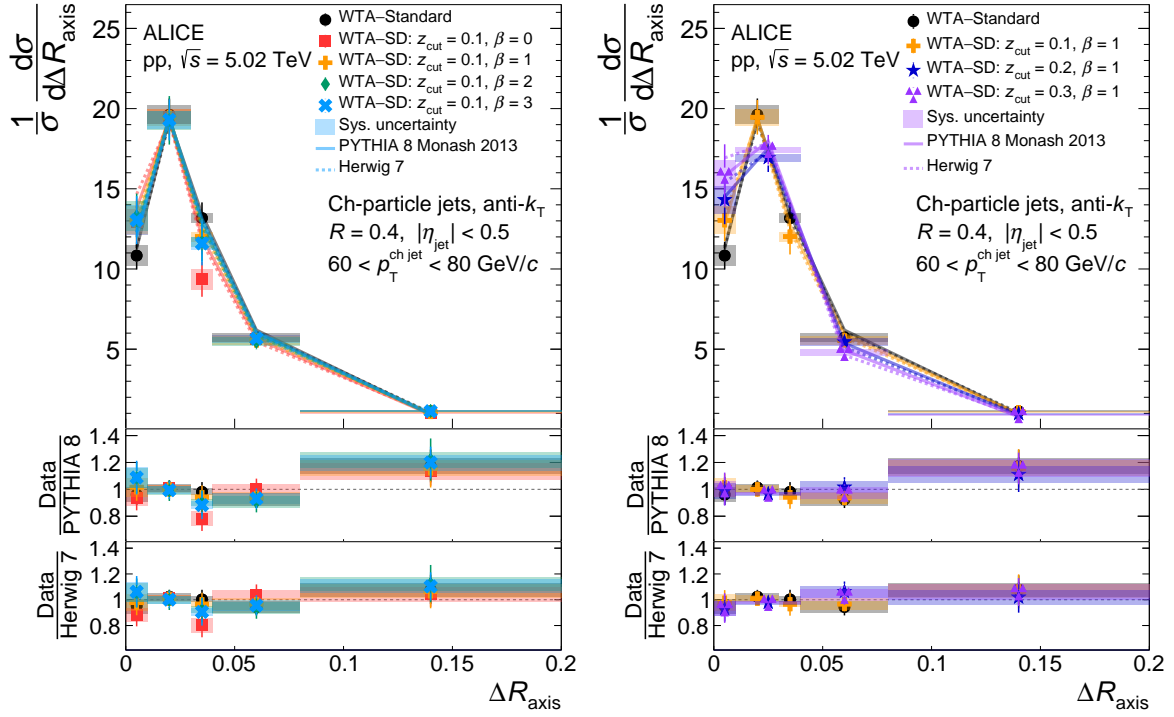


Figure A.3: Same as Figure A.1 for $60 < p_T^{\text{jet}} < 80$ GeV/c.

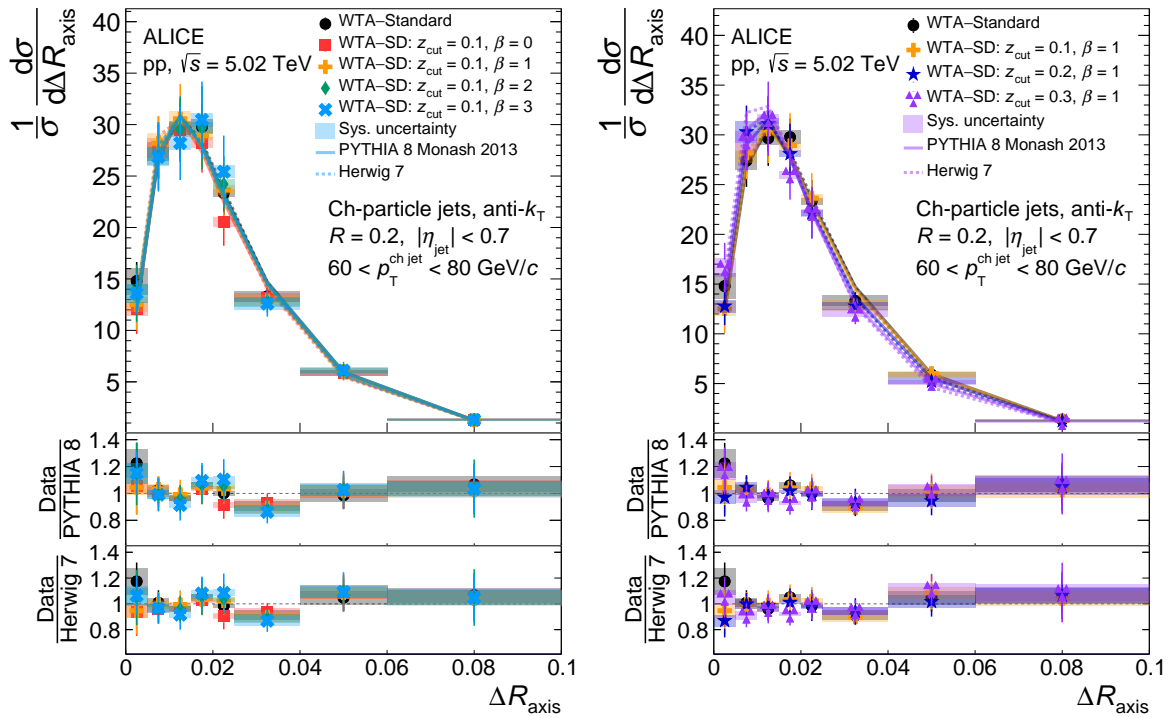
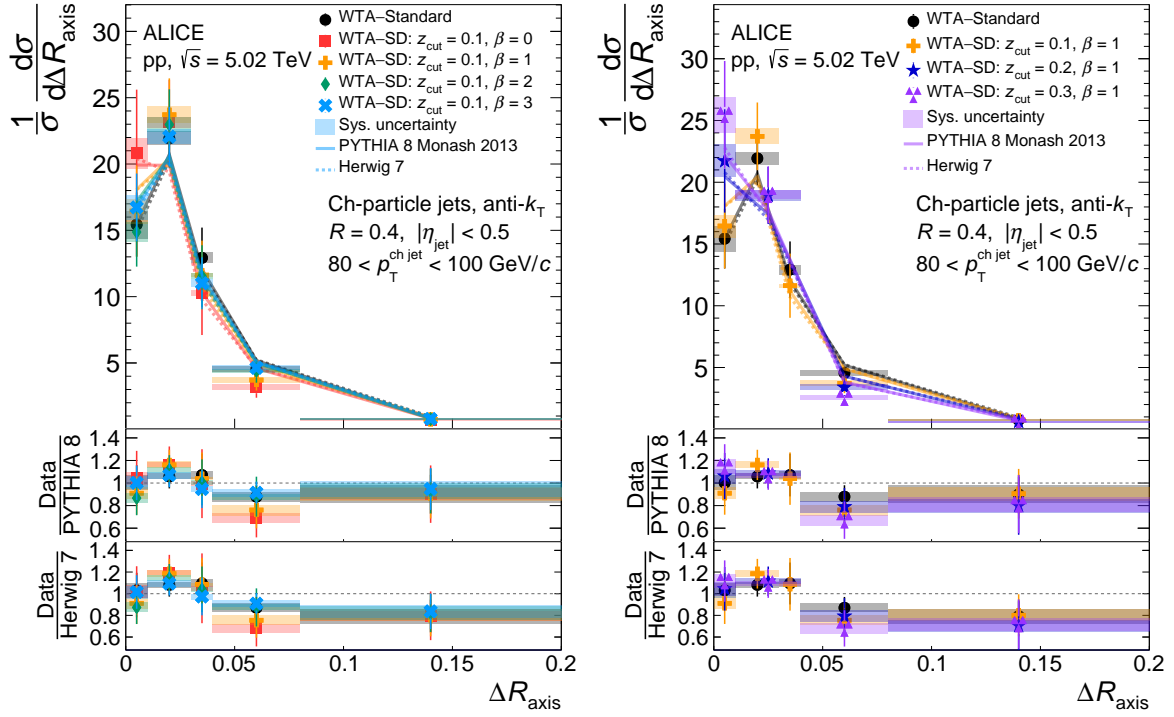
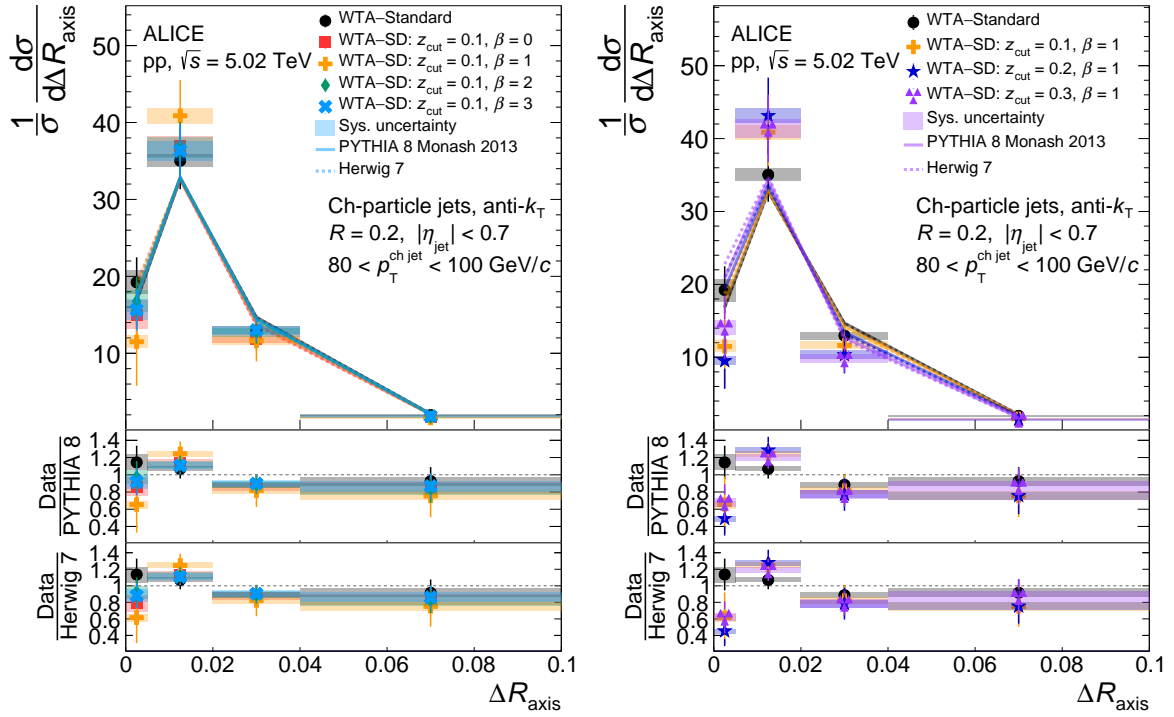


Figure A.4: Same as Figure A.1 for $R = 0.2$ for $60 < p_T^{\text{jet}} < 80$ GeV/c.

Figure A.5: Same as Figure A.1 for $80 < p_T^{\text{jet}} < 100$ GeV/c.Figure A.6: Same as Figure A.1 for $R = 0.2$ for $80 < p_T^{\text{jet}} < 100$ GeV/c.

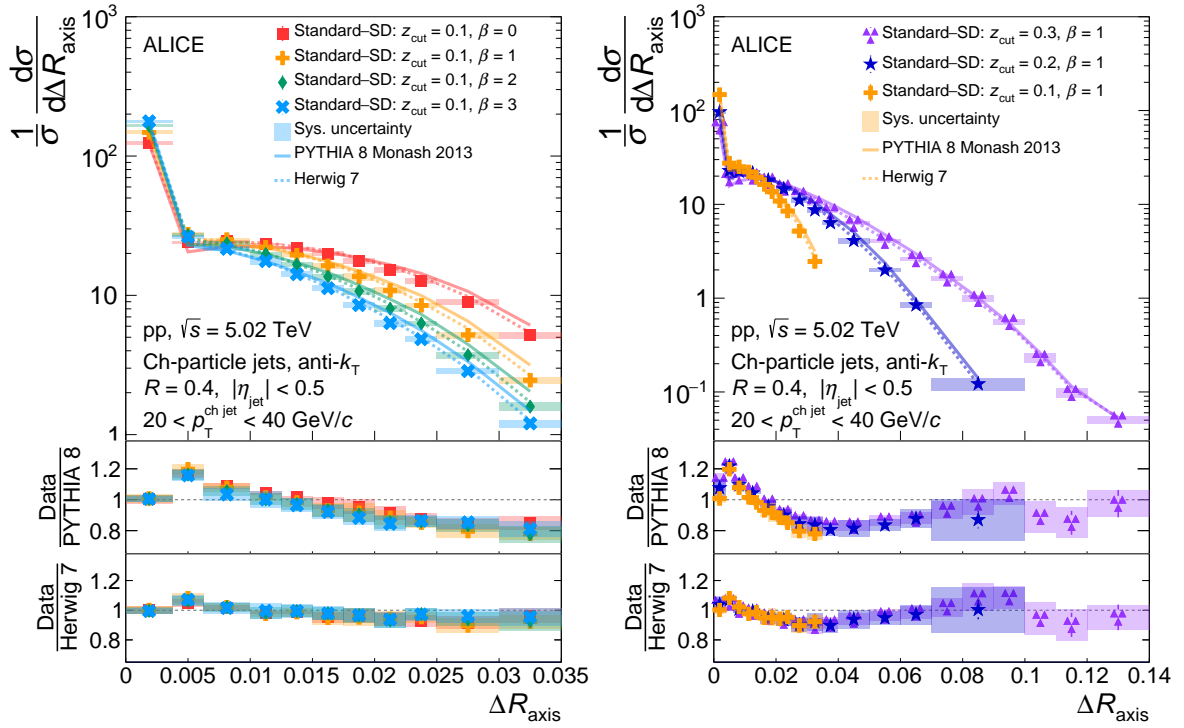


Figure A.7: Comparison between ΔR_{axis} Standard-SD measured distributions and Monte Carlo event generators for jets of $R = 0.4$ in $20 < p_T^{\text{jet}} < 40$ GeV/c. Left: distributions with $z_{\text{cut}} = 0.1$ and varying β . Right: distributions with $\beta = 1$ and varying z_{cut} .

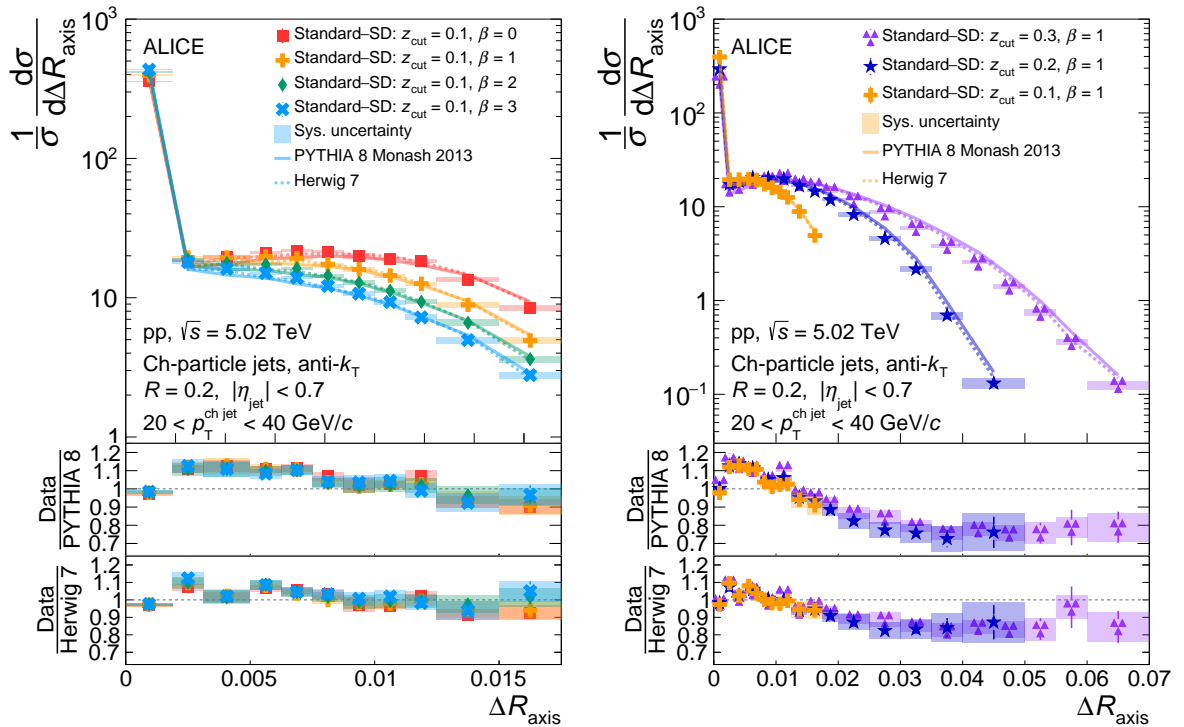


Figure A.8: Same as Figure A.7 for $R = 0.2$.

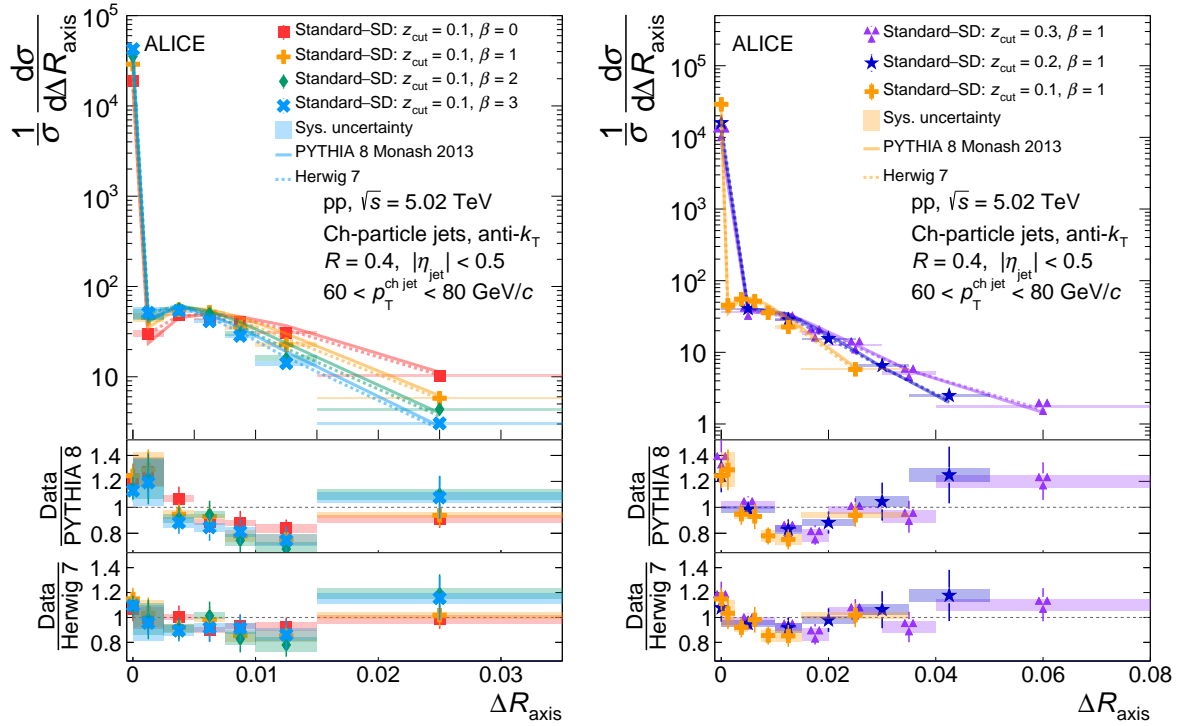


Figure A.9: Same as Figure A.7 for $60 < p_T^{\text{jet}} < 80$ GeV/c.

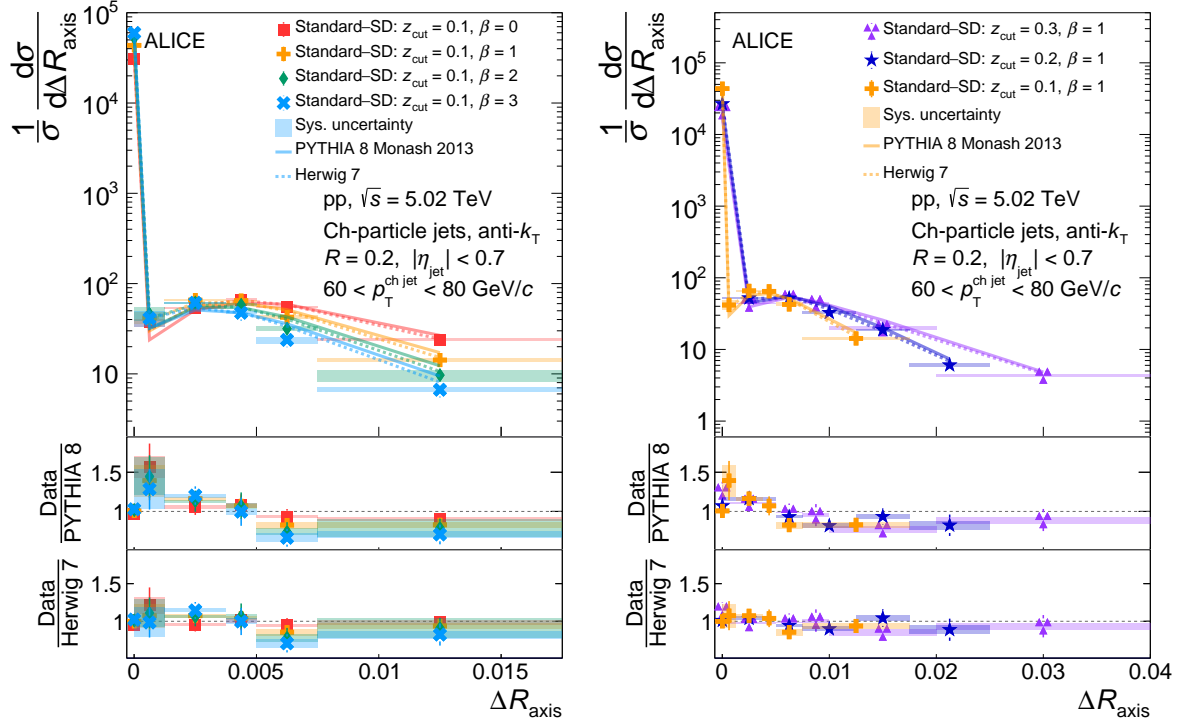


Figure A.10: Same as Figure A.7 for $R = 0.2$ for $60 < p_T^{\text{jet}} < 80$ GeV/c.

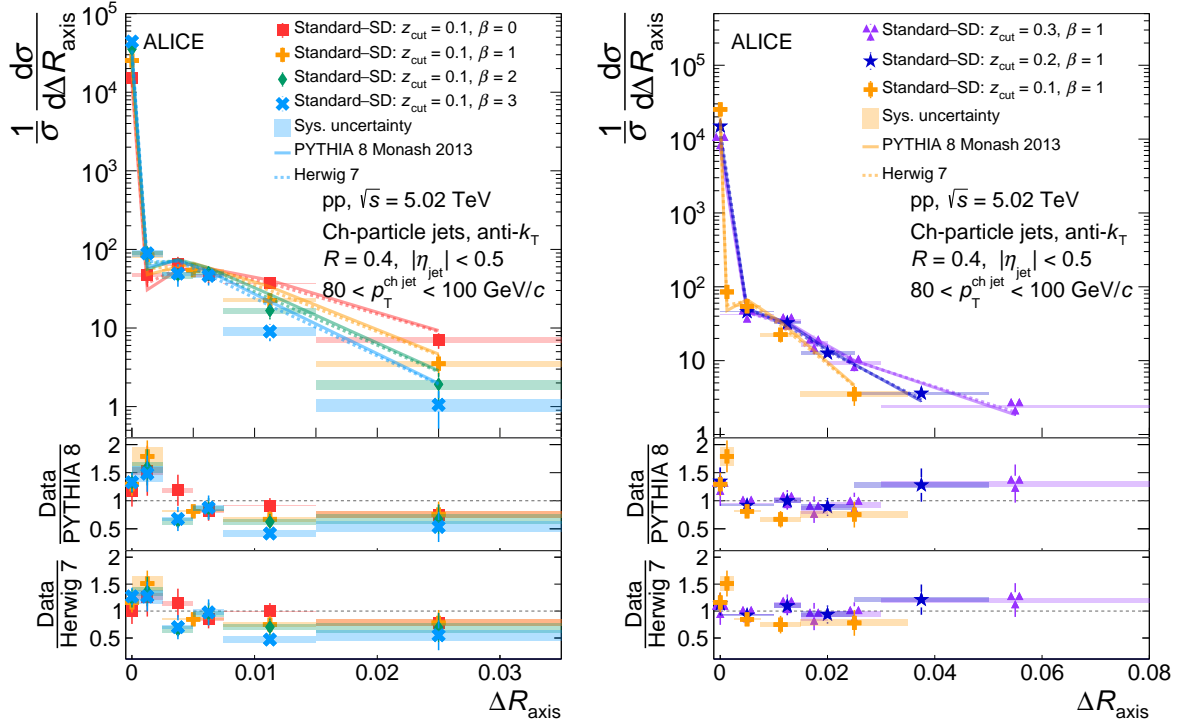


Figure A.11: Same as Figure A.7 for $80 < p_T^{\text{jet}} < 100$ GeV/c.

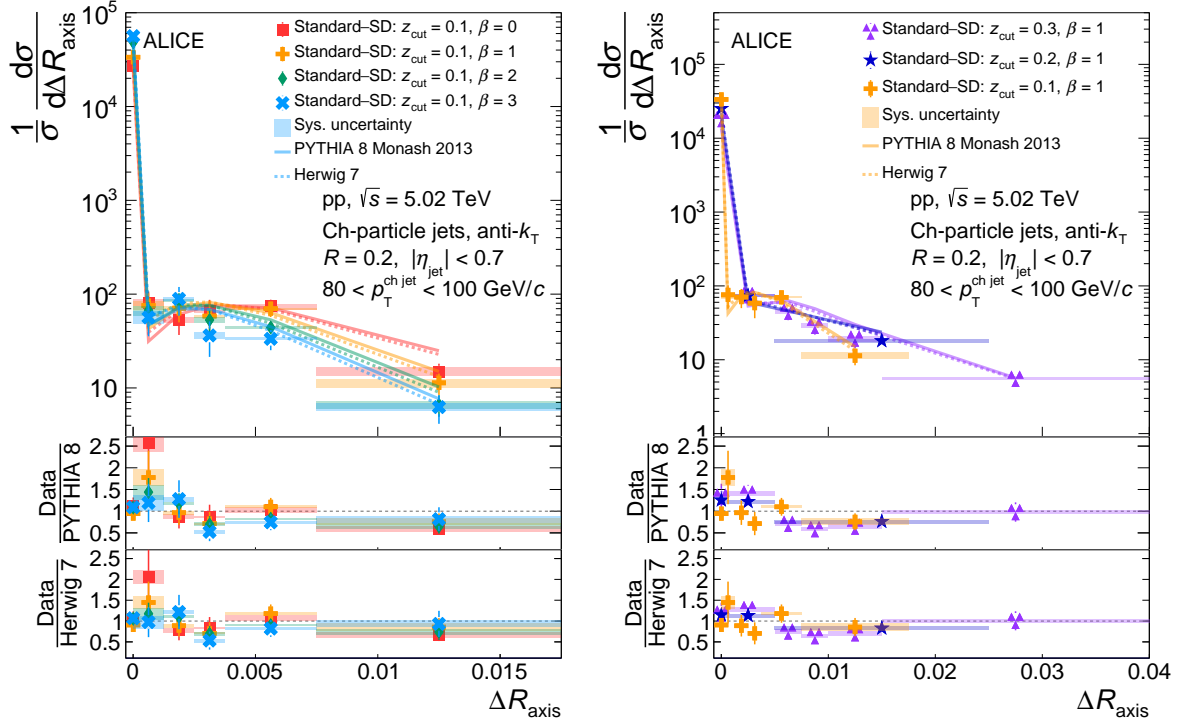


Figure A.12: Same as Figure A.7 for $R = 0.2$ for $80 < p_T^{\text{jet}} < 100$ GeV/c.

B Comparison to analytic predictions

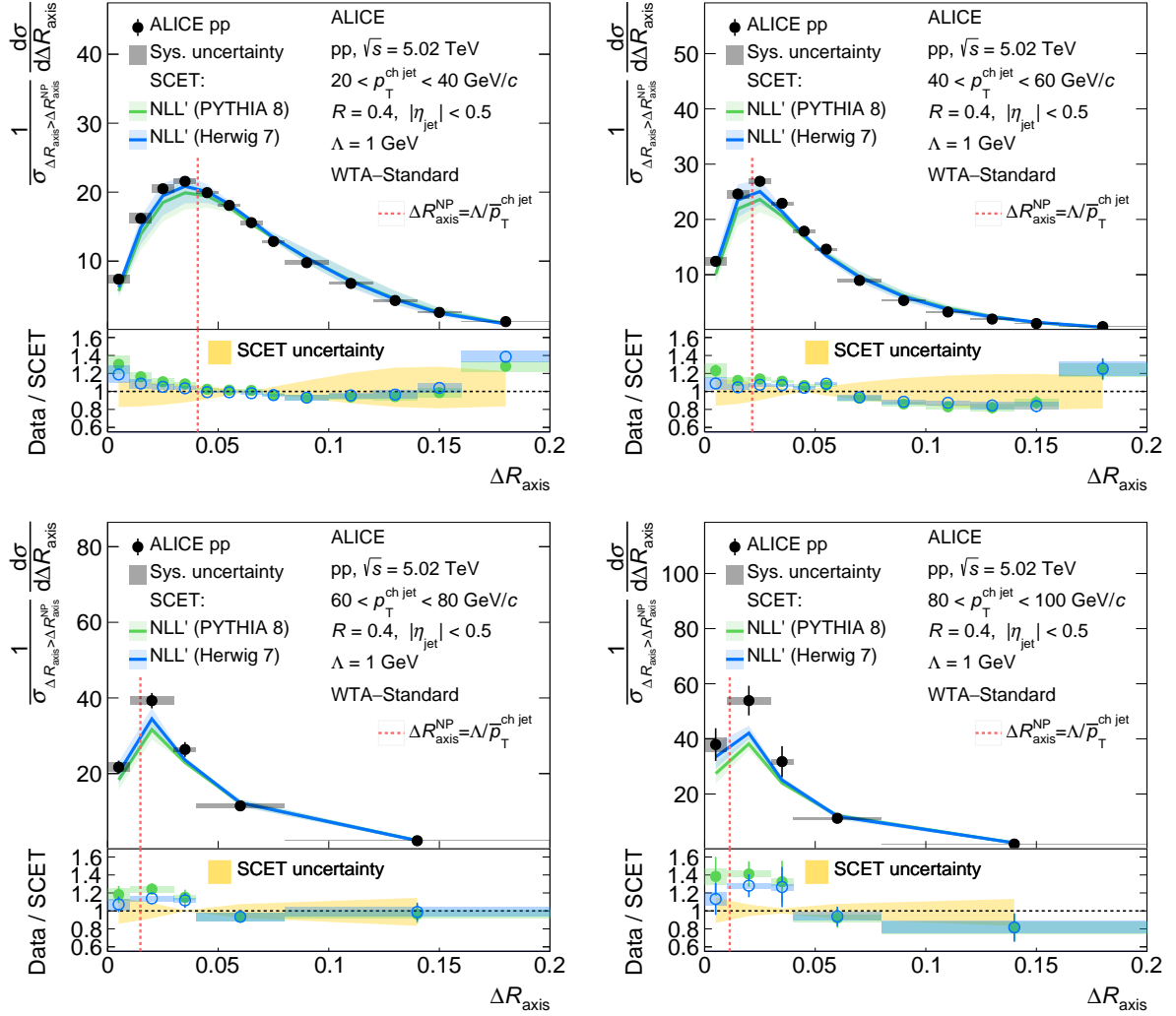


Figure B.1: Comparison between ΔR_{axis} measured distributions and analytic predictions for the WTA-Standard case with $R = 0.4$. Each panel corresponds to a different $p_{\text{T}}^{\text{ch,jet}}$ bin. The measured distribution is shown in black. The colored distributions correspond to the SCET prediction corrected with different MC event generators.

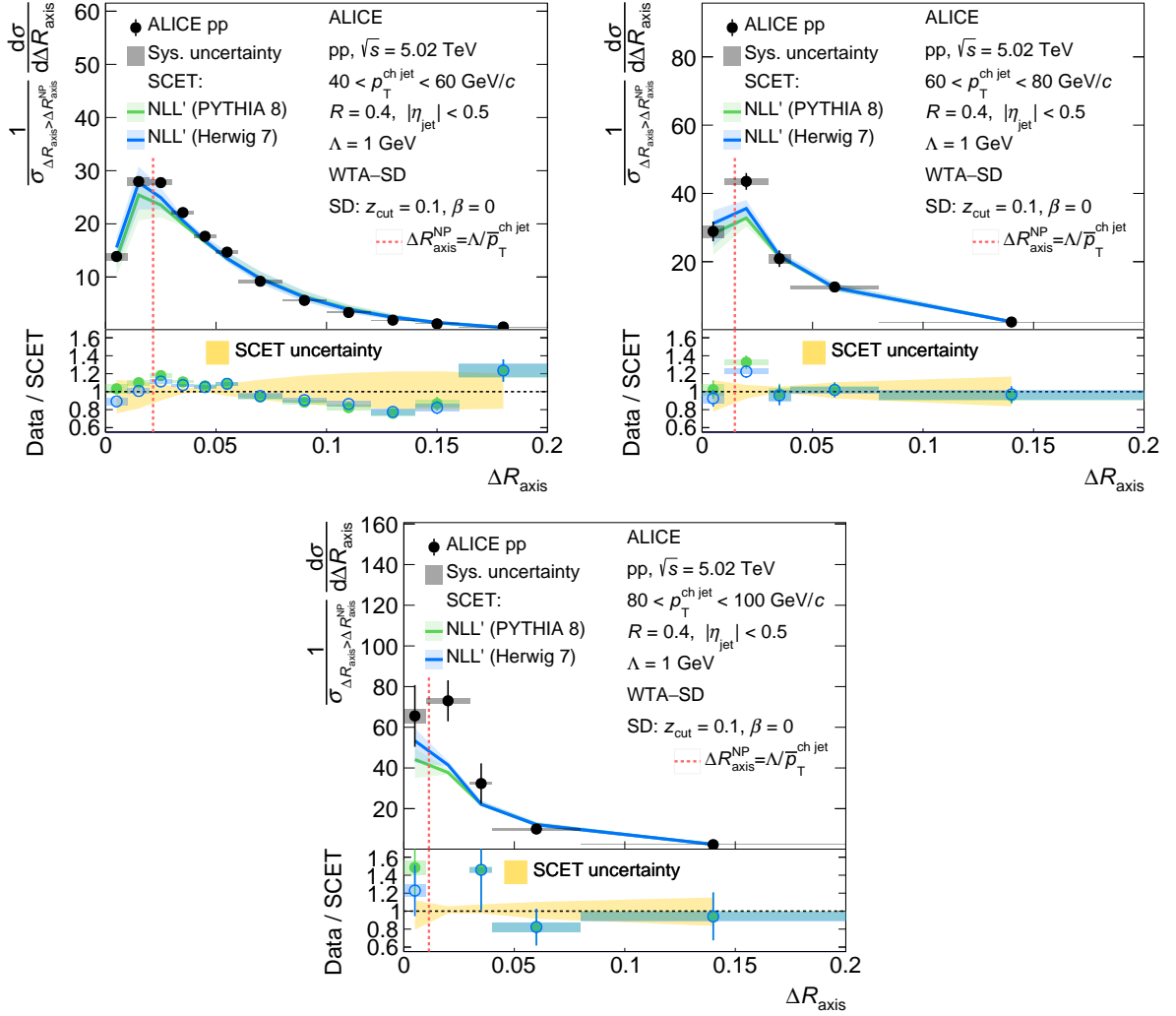


Figure B.2: Same as Figure B.1, for WTA-SD ($z_{\text{cut}} = 0.1, \beta = 0$) for $R = 0.4$.

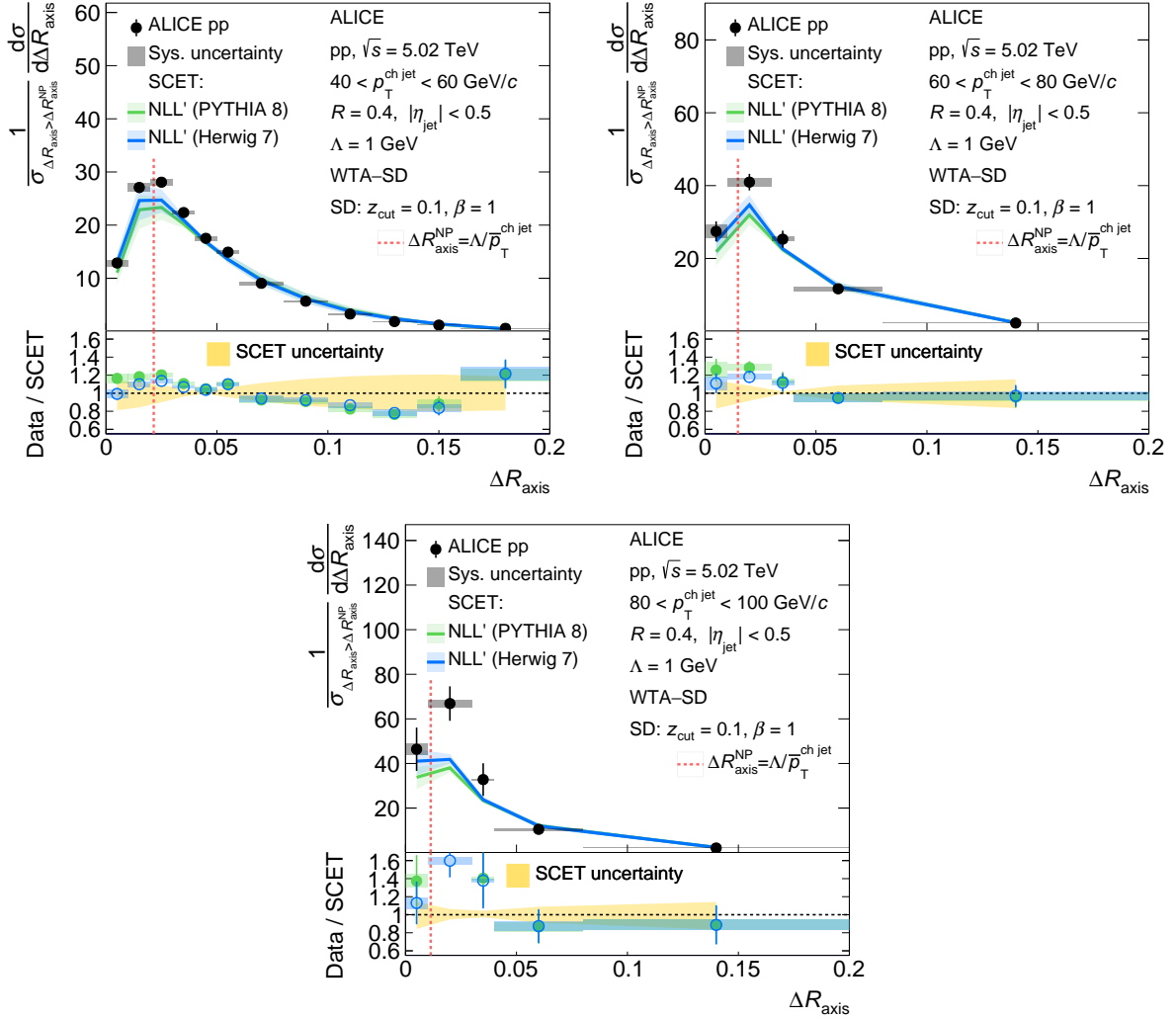


Figure B.3: Same as Figure B.1, for WTA-SD ($z_{\text{cut}} = 0.1, \beta = 1$) for $R = 0.4$.

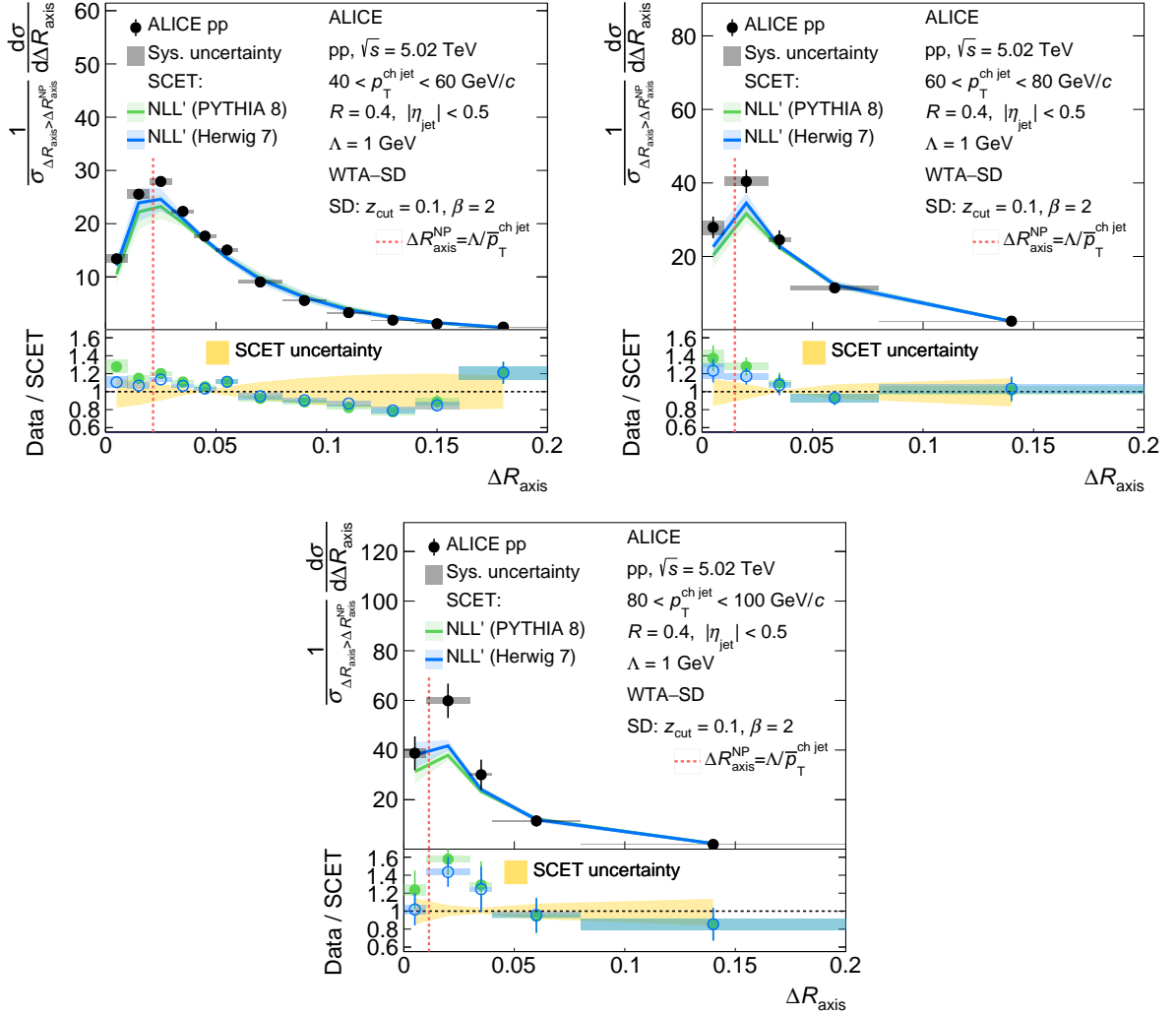


Figure B.4: Same as Figure B.1, for WTA-SD ($z_{\text{cut}} = 0.1, \beta = 2$) for $R = 0.4$.

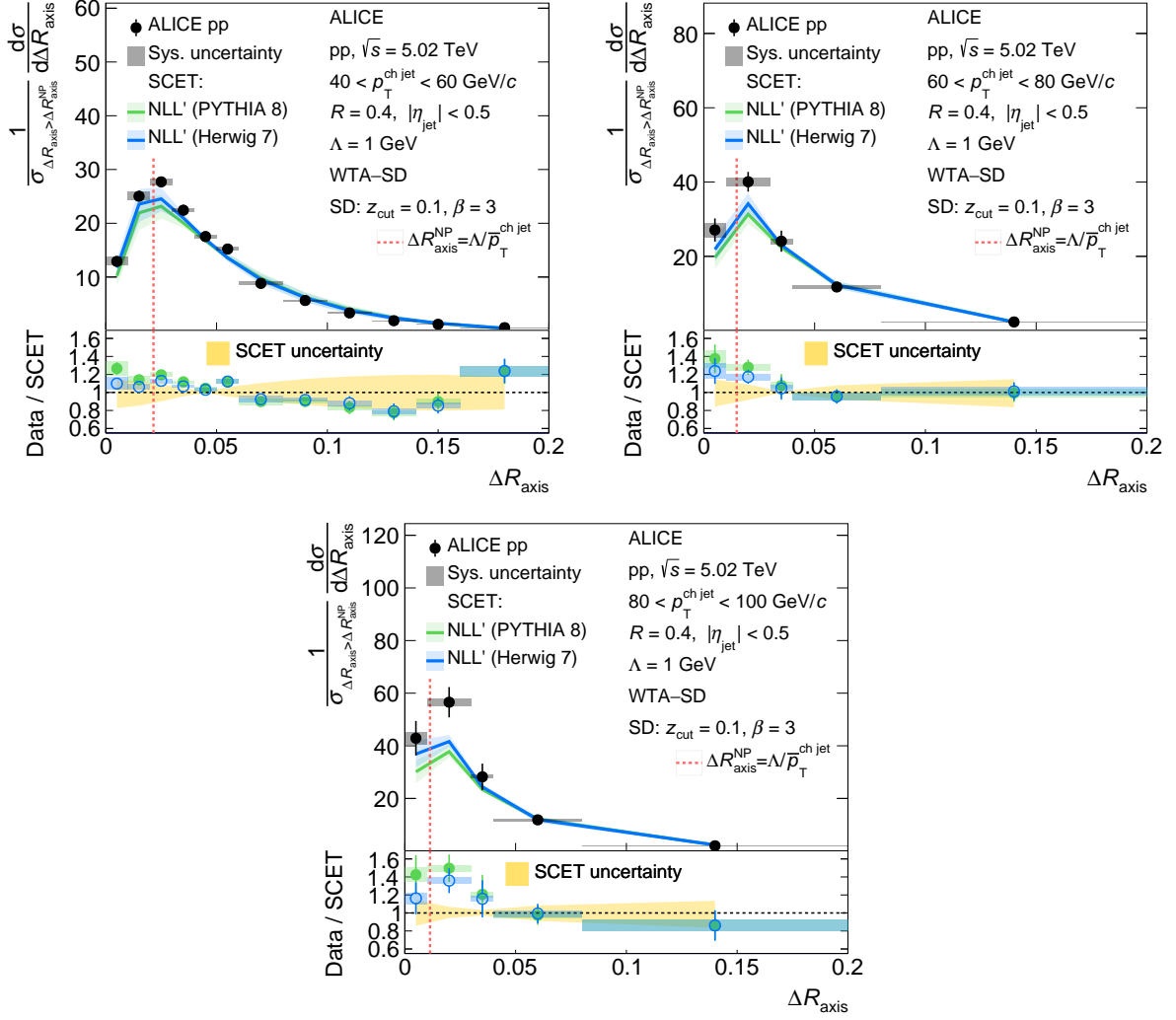


Figure B.5: Same as Figure B.1, for WTA-SD ($z_{\text{cut}} = 0.1, \beta = 3$) for $R = 0.4$.

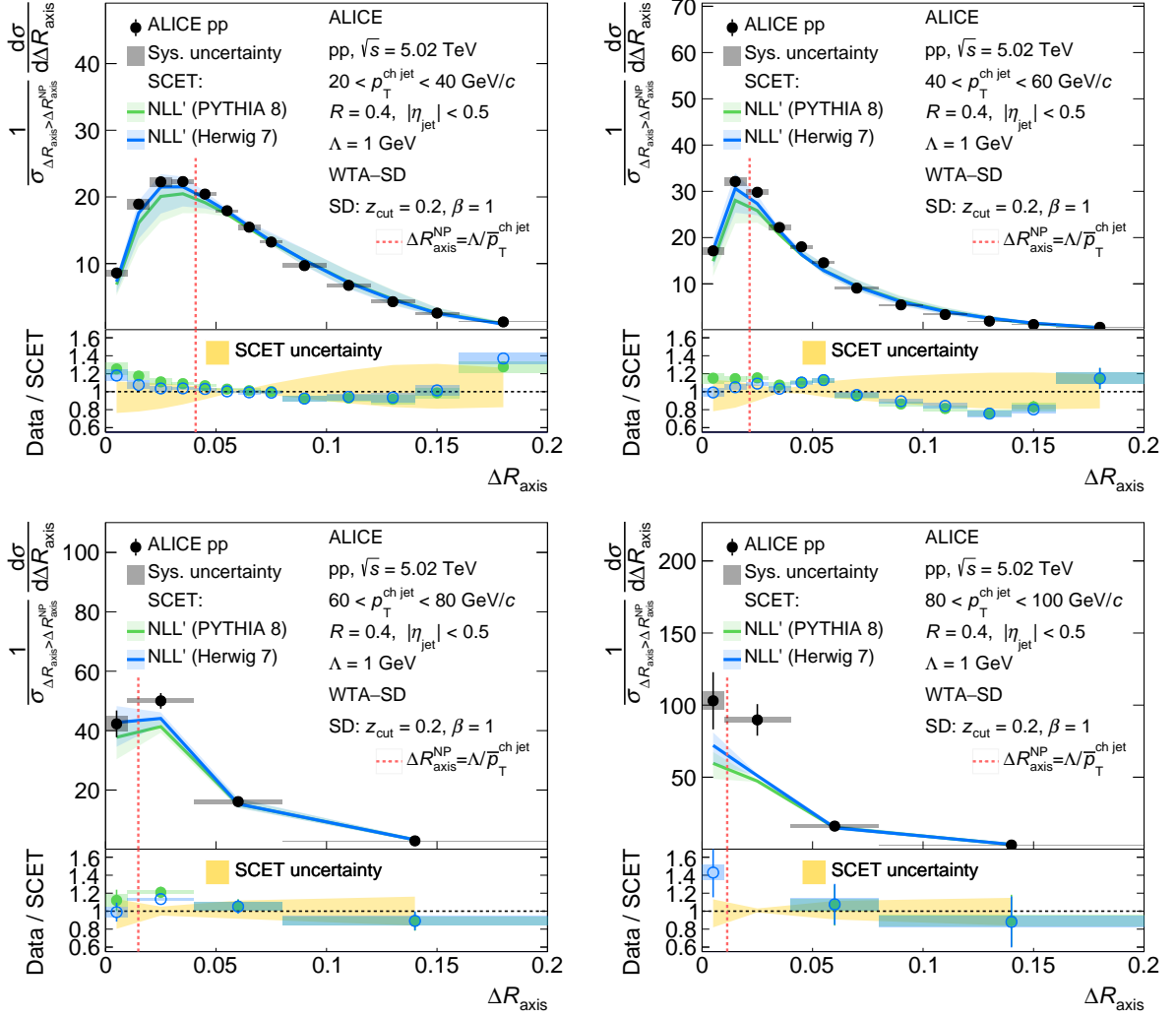


Figure B.6: Same as Figure B.1, for WTA-SD ($z_{\text{cut}} = 0.2, \beta = 1$) for $R = 0.4$.

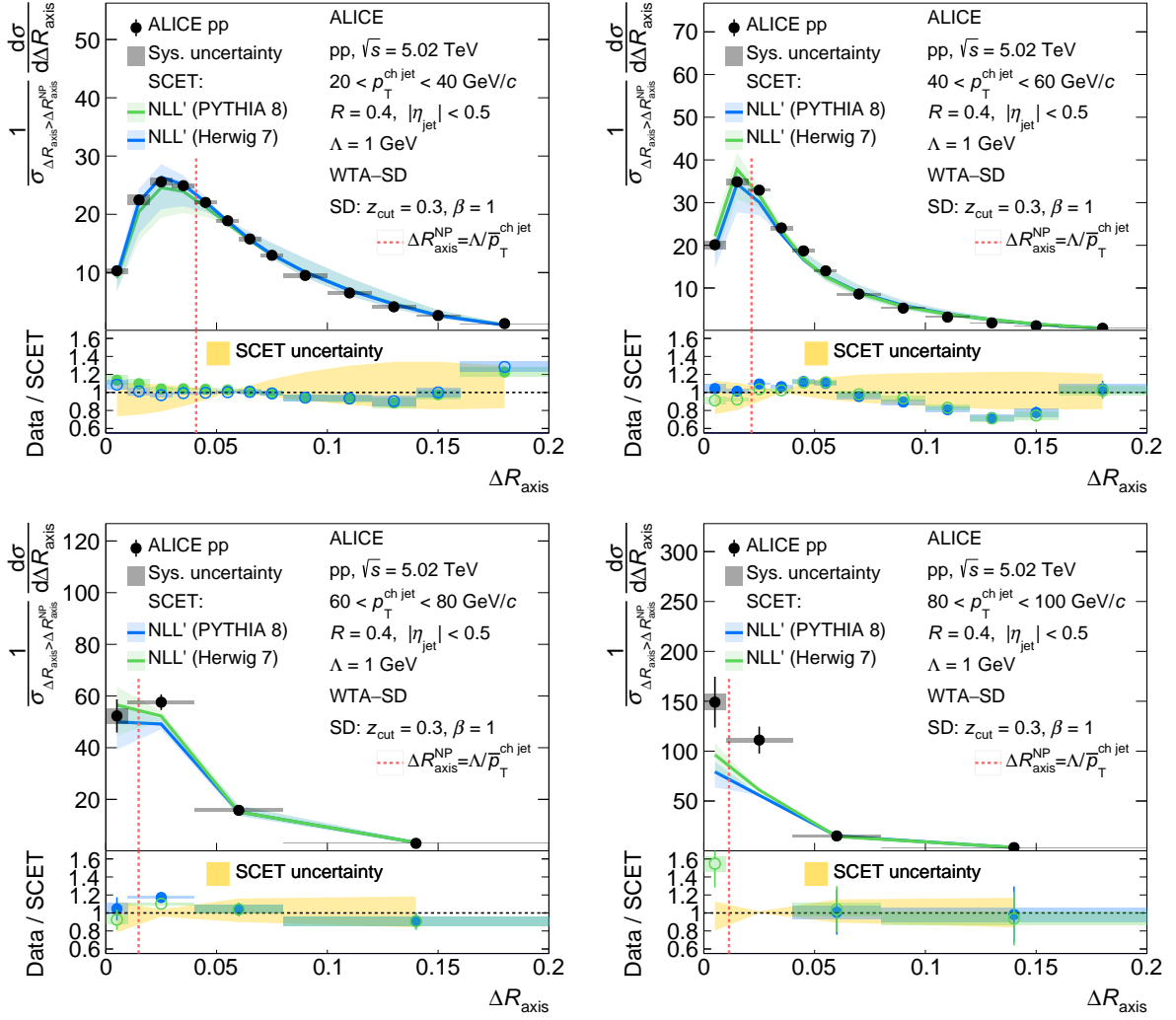


Figure B.7: Same as Figure B.1, for WTA-SD ($z_{\text{cut}} = 0.3, \beta = 1$) for $R = 0.4$.

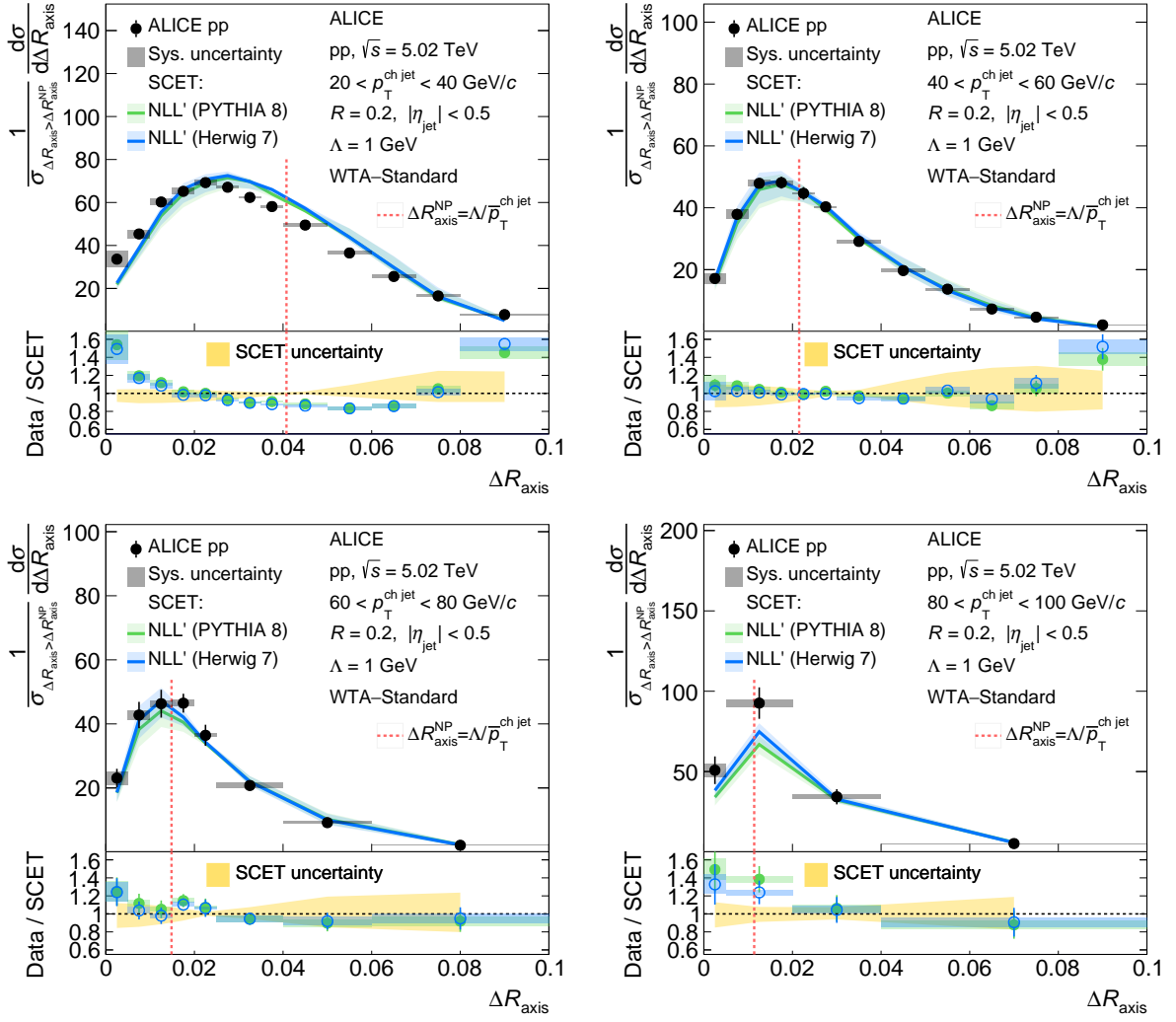


Figure B.8: Same as Figure B.1, for WTA-Standard for $R = 0.2$.

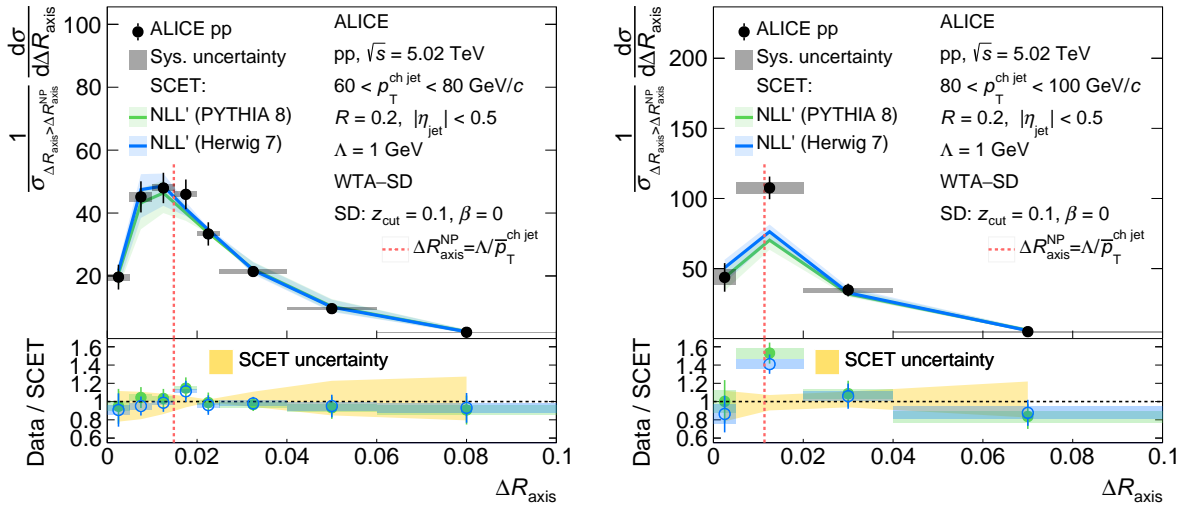


Figure B.9: Same as Figure B.1, for WTA-SD ($z_{\text{cut}} = 0.1, \beta = 0$) for $R = 0.2$.

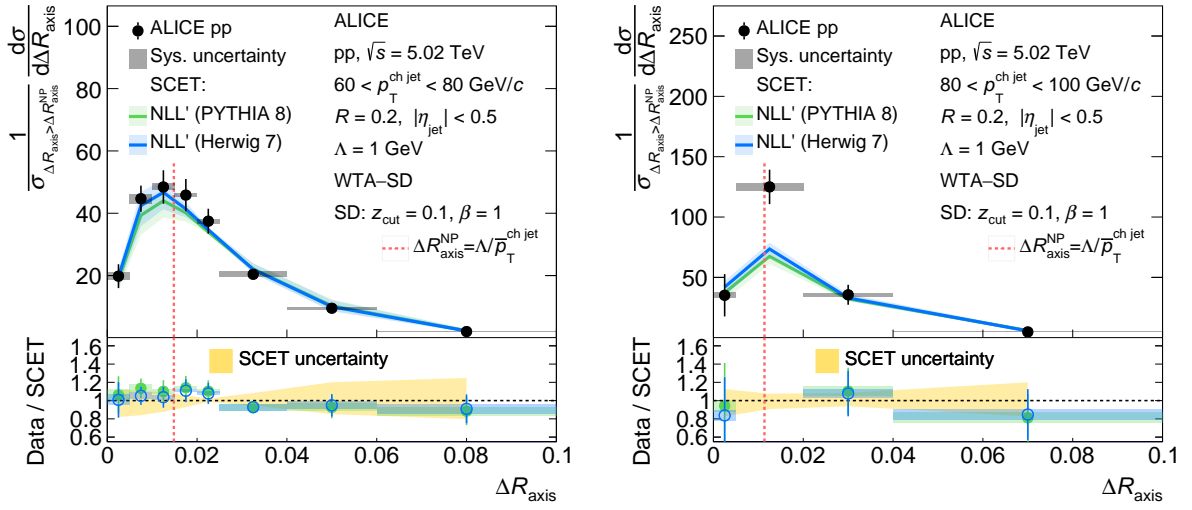


Figure B.10: Same as Figure B.1, for WTA–SD ($z_{\text{cut}} = 0.1$, $\beta = 1$) for $R = 0.2$.

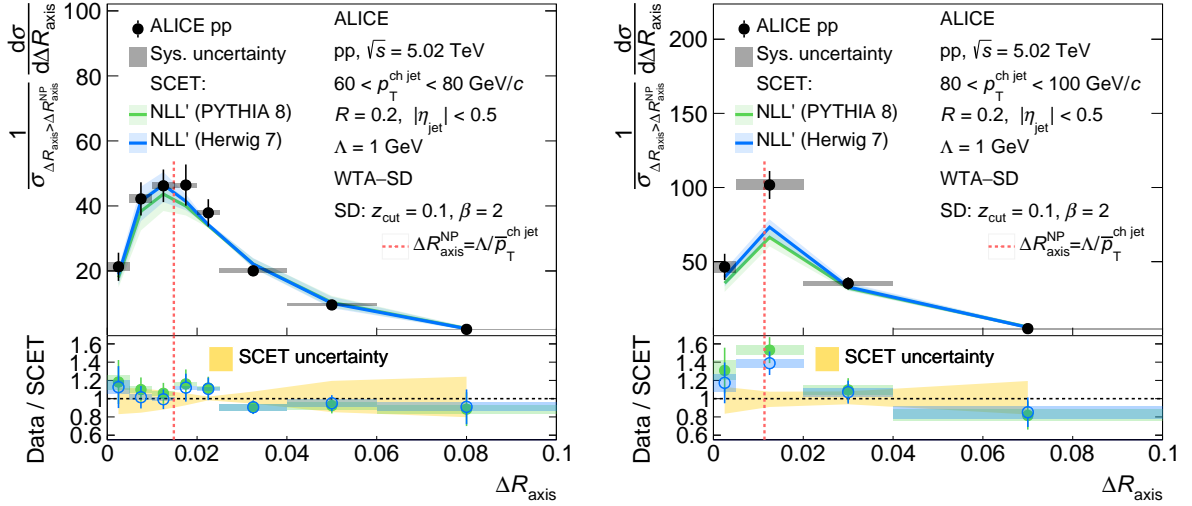


Figure B.11: Same as Figure B.1, for WTA–SD ($z_{\text{cut}} = 0.1$, $\beta = 2$) for $R = 0.2$.

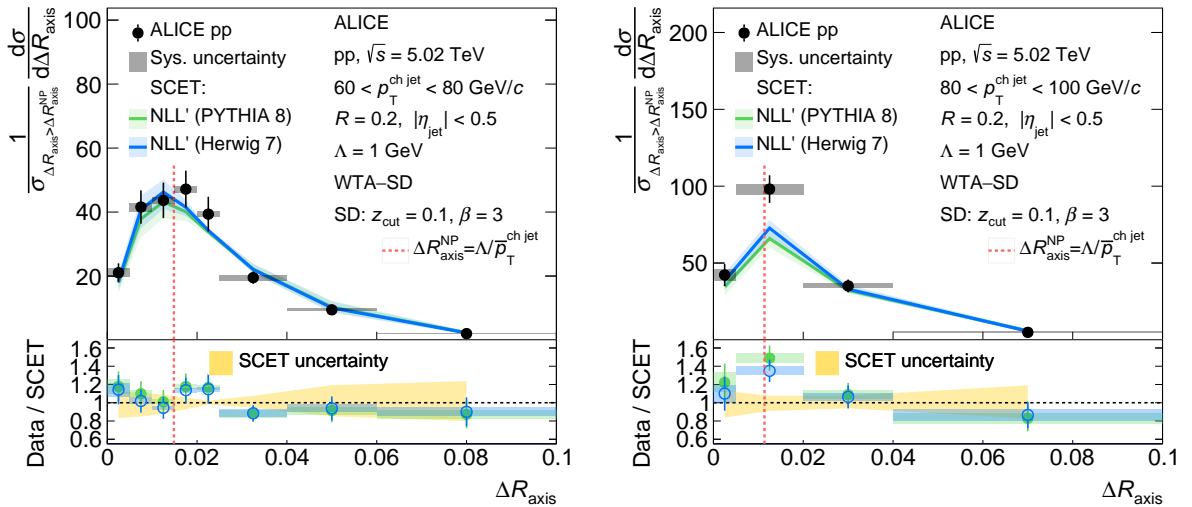


Figure B.12: Same as Figure B.1, for WTA–SD ($z_{\text{cut}} = 0.1$, $\beta = 3$) for $R = 0.2$.

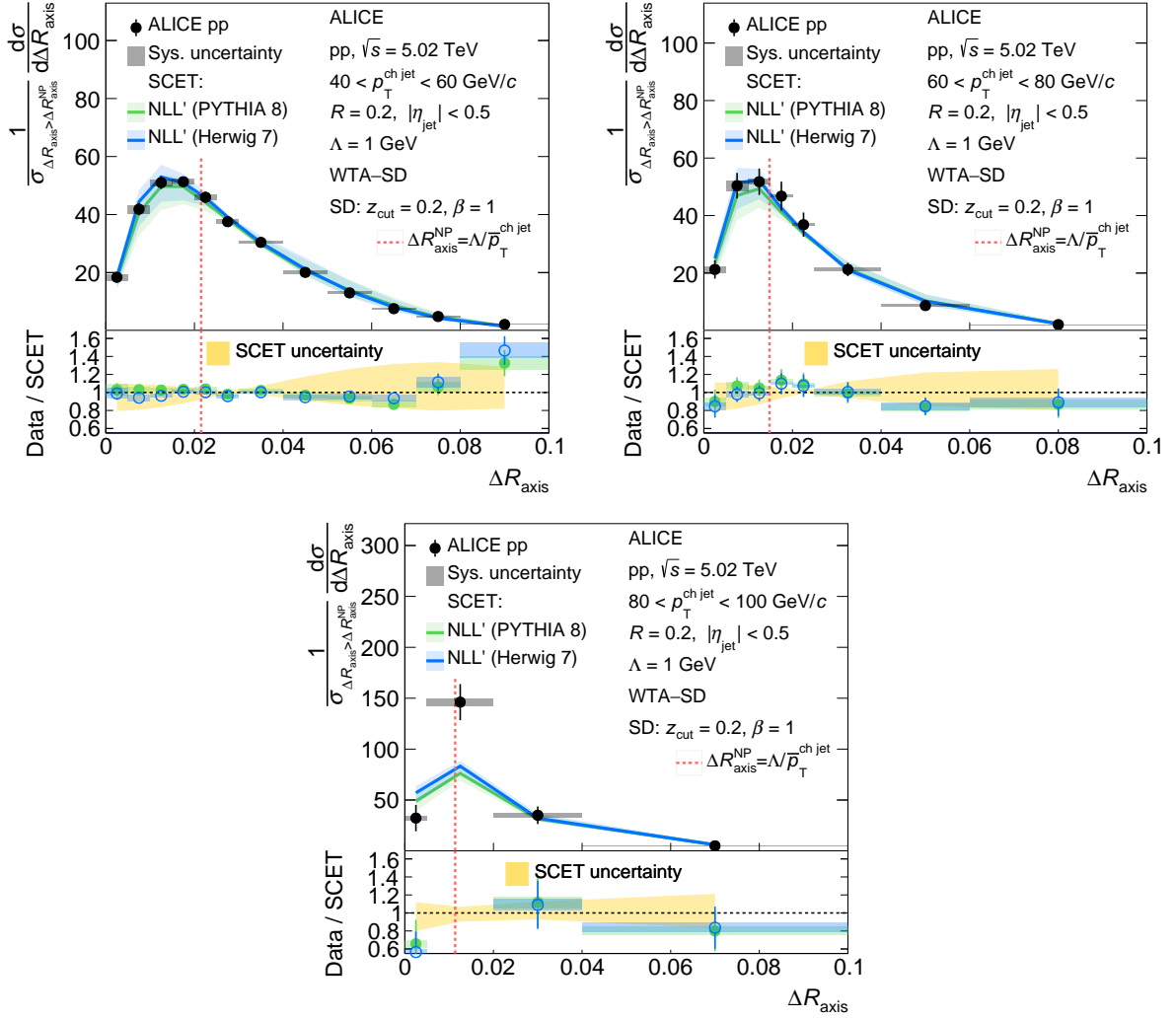


Figure B.13: Same as Figure B.1, for WTA-SD ($z_{\text{cut}} = 0.2, \beta = 1$) for $R = 0.2$.

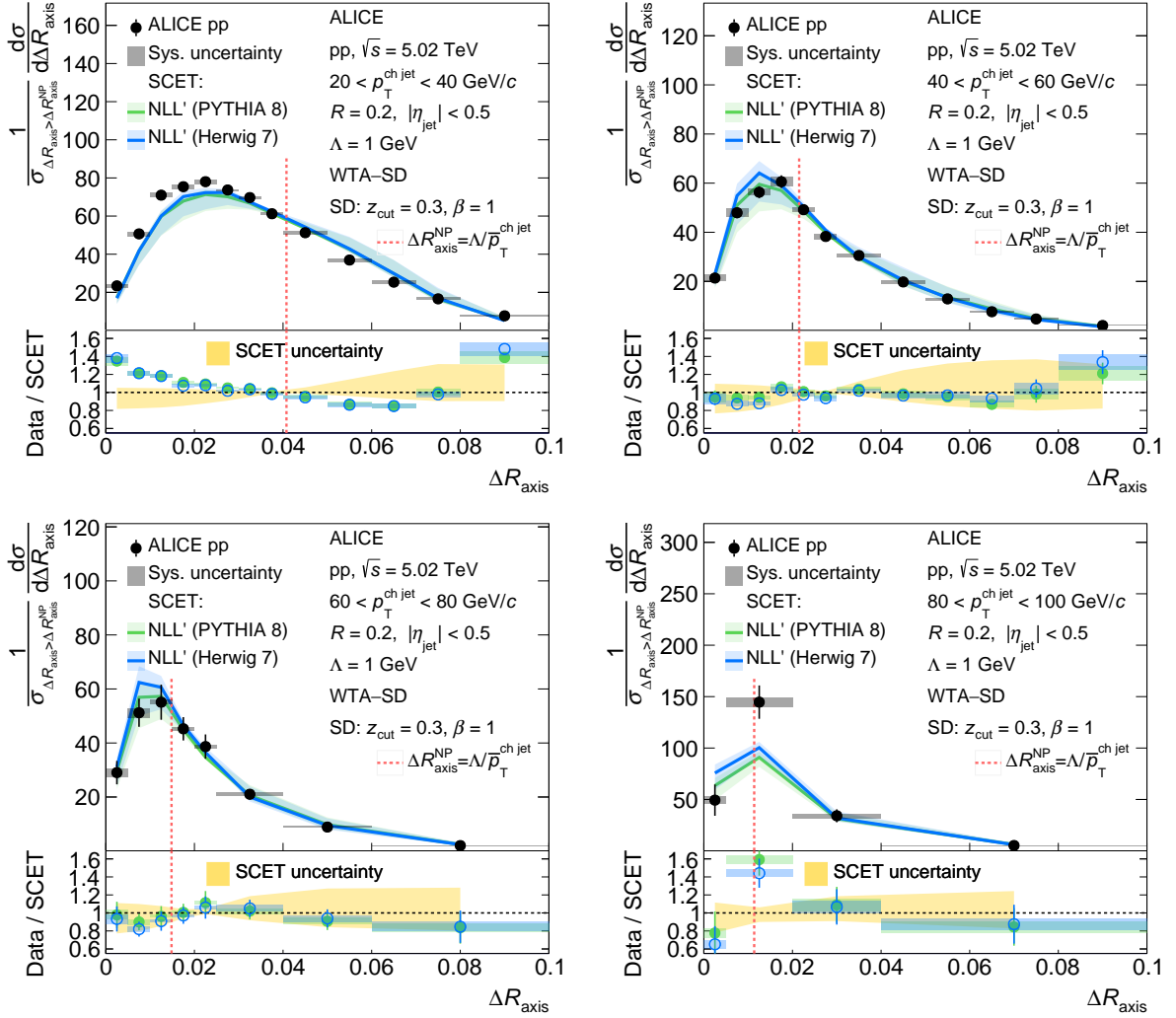










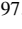


Figure B.14: Same as Figure B.1, for WTA-SD ($z_{\text{cut}} = 0.3, \beta = 1$) for $R = 0.2$.

C The ALICE Collaboration

S. Acharya ¹²⁵, D. Adamová ⁸⁶, A. Adler⁶⁹, G. Aglieri Rinella ³², M. Agnello ²⁹, N. Agrawal ⁵⁰, Z. Ahammed ¹³², S. Ahmad ¹⁵, S.U. Ahn ⁷⁰, I. Ahuja ³⁷, A. Akindinov ¹⁴⁰, M. Al-Turany ⁹⁷, D. Aleksandrov ¹⁴⁰, B. Alessandro ⁵⁵, H.M. Alfanda ⁶, R. Alfaro Molina ⁶⁶, B. Ali ¹⁵, A. Alici ²⁵, N. Alizadehvandchali ¹¹⁴, A. Alkin ³², J. Alme ²⁰, G. Alocco ⁵¹, T. Alt ⁶³, I. Altsybeev ¹⁴⁰, M.N. Anaam ⁶, C. Andrei ⁴⁵, A. Andronic ¹³⁵, V. Anguelov ⁹⁴, F. Antinori ⁵³, P. Antonioli ⁵⁰, N. Apadula ⁷⁴, L. Aphecetche ¹⁰³, H. Appelshäuser ⁶³, C. Arata ⁷³, S. Arcelli ²⁵, M. Aresti ⁵¹, R. Arnaldi ⁵⁵, J.G.M.C.A. Arneiro ¹¹⁰, I.C. Arsene ¹⁹, M. Arslanok ¹³⁷, A. Augustinus ³², R. Averbeck ⁹⁷, M.D. Azmi ¹⁵, A. Badalà ⁵², J. Bae ¹⁰⁴, Y.W. Baek ⁴⁰, X. Bai ¹¹⁸, R. Bailhache ⁶³, Y. Bailung ⁴⁷, A. Balbino ²⁹, A. Baldisseri ¹²⁸, B. Balis ², D. Banerjee ⁴, Z. Banoo ⁹¹, R. Barbera ²⁶, F. Barile ³¹, L. Barioglio ⁹⁵, M. Barlou⁷⁸, G.G. Barnaföldi ¹³⁶, L.S. Barnby ⁸⁵, V. Barret ¹²⁵, L. Barreto ¹¹⁰, C. Bartels ¹¹⁷, K. Barth ³², E. Bartsch ⁶³, N. Bastid ¹²⁵, S. Basu ⁷⁵, G. Batigne ¹⁰³, D. Battistini ⁹⁵, B. Batyunya ¹⁴¹, D. Bauri⁴⁶, J.L. Bazo Alba ¹⁰¹, I.G. Bearden ⁸³, C. Beattie ¹³⁷, P. Becht ⁹⁷, D. Behera ⁴⁷, I. Belikov ¹²⁷, A.D.C. Bell Hechavarria ¹³⁵, F. Bellini ²⁵, R. Bellwied ¹¹⁴, S. Belokurova ¹⁴⁰, V. Belyaev ¹⁴⁰, G. Bencedi ¹³⁶, S. Beole ²⁴, A. Bercuci ⁴⁵, Y. Berdnikov ¹⁴⁰, A. Berdnikova ⁹⁴, L. Bergmann ⁹⁴, M.G. Besoiu ⁶², L. Betev ³², P.P. Bhaduri ¹³², A. Bhasin ⁹¹, M.A. Bhat ⁴, B. Bhattacharjee ⁴¹, L. Bianchi ²⁴, N. Bianchi ⁴⁸, J. Bielčik ³⁵, J. Bielčiková ⁸⁶, J. Biernat ¹⁰⁷, A.P. Bigot ¹²⁷, A. Bilandzic ⁹⁵, G. Biro ¹³⁶, S. Biswas ⁴, N. Bize ¹⁰³, J.T. Blair ¹⁰⁸, D. Blau ¹⁴⁰, M.B. Blidaru ⁹⁷, N. Bluhme³⁸, C. Blume ⁶³, G. Boca ^{21,54}, F. Bock ⁸⁷, T. Bodova ²⁰, A. Bogdanov¹⁴⁰, S. Boi ²², J. Bok ⁵⁷, L. Boldizsár ¹³⁶, A. Bolozdynya ¹⁴⁰, M. Bombara ³⁷, P.M. Bond ³², G. Bonomi ^{131,54}, H. Borel ¹²⁸, A. Borissov ¹⁴⁰, A.G. Borquez Carcamo ⁹⁴, H. Bossi ¹³⁷, E. Botta ²⁴, Y.E.M. Bouziani ⁶³, L. Bratrud ⁶³, P. Braun-Munzinger ⁹⁷, M. Bregant ¹¹⁰, M. Broz ³⁵, G.E. Bruno ^{96,31}, M.D. Buckland ²³, D. Budnikov ¹⁴⁰, H. Buesching ⁶³, S. Bufalino ²⁹, O. Bugnon¹⁰³, P. Buhler ¹⁰², Z. Buthelezi ^{67,121}, S.A. Bysiak¹⁰⁷, M. Cai ⁶, H. Caines ¹³⁷, A. Caliva ⁹⁷, E. Calvo Villar ¹⁰¹, J.M.M. Camacho ¹⁰⁹, P. Camerini ²³, F.D.M. Canedo ¹¹⁰, M. Carabas ¹²⁴, A.A. Carballo ³², F. Carnesecchi ³², R. Caron ¹²⁶, L.A.D. Carvalho ¹¹⁰, J. Castillo Castellanos ¹²⁸, F. Catalano ^{24,29}, C. Ceballos Sanchez ¹⁴¹, I. Chakaberia ⁷⁴, P. Chakraborty ⁴⁶, S. Chandra ¹³², S. Chapeland ³², M. Chartier ¹¹⁷, S. Chattopadhyay ¹³², S. Chattopadhyay ⁹⁹, T.G. Chavez ⁴⁴, T. Cheng ^{97,6}, C. Cheshkov ¹²⁶, B. Cheynis ¹²⁶, V. Chibante Barroso ³², D.D. Chinellato ¹¹¹, E.S. Chizzali ^{11,95}, J. Cho ⁵⁷, S. Cho ⁵⁷, P. Chochula ³², P. Christakoglou ⁸⁴, C.H. Christensen ⁸³, P. Christiansen ⁷⁵, T. Chujo ¹²³, M. Ciacco ²⁹, C. Cicalo ⁵¹, F. Cindolo ⁵⁰, M.R. Ciupek⁹⁷, G. Clai^{III,50}, F. Colamaria ⁴⁹, J.S. Colburn¹⁰⁰, D. Colella ^{96,31}, M. Colocci ³², M. Concas ^{IV,55}, G. Conesa Balbastre ⁷³, Z. Conesa del Valle ⁷², G. Contin ²³, J.G. Contreras ³⁵, M.L. Coquet ¹²⁸, T.M. Cormier^{I,87}, P. Cortese ^{130,55}, M.R. Cosentino ¹¹², F. Costa ³², S. Costanza ^{21,54}, C. Cot ⁷², J. Crkovská ⁹⁴, P. Crochet ¹²⁵, R. Cruz-Torres ⁷⁴, E. Cuautle⁶⁴, P. Cui ⁶, A. Dainese ⁵³, M.C. Danisch ⁹⁴, A. Danu ⁶², P. Das ⁸⁰, P. Das ⁴, S. Das ⁴, A.R. Dash ¹³⁵, S. Dash ⁴⁶, A. De Caro ²⁸, G. de Cataldo ⁴⁹, J. de Cuveland³⁸, A. De Falco ²², D. De Gruttola ²⁸, N. De Marco ⁵⁵, C. De Martin ²³, S. De Pasquale ²⁸, S. Deb ⁴⁷, R.J. Debski ², K.R. Deja ¹³³, R. Del Grande ⁹⁵, L. Dello Stritto ²⁸, W. Deng ⁶, P. Dhankher ¹⁸, D. Di Bari ³¹, A. Di Mauro ³², R.A. Diaz ^{141,7}, T. Dietel ¹¹³, Y. Ding ^{126,6}, R. Divià ³², D.U. Dixit ¹⁸, Ø. Djuvsland²⁰, U. Dmitrieva ¹⁴⁰, A. Dobrin ⁶², B. Dönigus ⁶³, J.M. Dubinski¹³³, A. Dubla ⁹⁷, S. Dudi ⁹⁰, P. Dupieux ¹²⁵, M. Durkac¹⁰⁶, N. Dzalaiova¹², T.M. Eder ¹³⁵, R.J. Ehlers ⁸⁷, V.N. Eikeland²⁰, F. Eisenhut ⁶³, D. Elia ⁴⁹, B. Erasmus ¹⁰³, F. Ercolessi ²⁵, F. Erhardt ⁸⁹, M.R. Ersdal²⁰, B. Espagnon ⁷², G. Eulisse ³², D. Evans ¹⁰⁰, S. Evdokimov ¹⁴⁰, L. Fabbietti ⁹⁵, M. Faggin ²⁷, J. Faivre ⁷³, F. Fan ⁶, W. Fan ⁷⁴, A. Fantoni ⁴⁸, M. Fasel ⁸⁷, P. Fedchio²⁹, A. Feliciello ⁵⁵, G. Feofilov ¹⁴⁰, A. Fernández Téllez ⁴⁴, L. Ferrandi ¹¹⁰, M.B. Ferrer ³², A. Ferrero ¹²⁸, C. Ferrero ⁵⁵, A. Ferretti ²⁴, V.J.G. Feuillard ⁹⁴, V. Filova³⁵, D. Finogeev ¹⁴⁰, F.M. Fionda ⁵¹, F. Flor ¹¹⁴, A.N. Flores ¹⁰⁸, S. Foertsch ⁶⁷, I. Fokin ⁹⁴, S. Fokin ¹⁴⁰, E. Fragiaco ⁵⁶, E. Frajna ¹³⁶, U. Fuchs ³², N. Funicello ²⁸, C. Furget ⁷³, A. Furs ¹⁴⁰, T. Fusayasu ⁹⁸, J.J. Gaardhøje ⁸³, M. Gagliardi ²⁴, A.M. Gago ¹⁰¹, C.D. Galvan ¹⁰⁹, D.R. Gangadharan ¹¹⁴, P. Ganoti ⁷⁸, C. Garabatos ⁹⁷, J.R.A. Garcia ⁴⁴, E. Garcia-Solis ⁹, K. Garg ¹⁰³, C. Gargiulo ³², A. Garibli⁸¹, K. Garner¹³⁵, P. Gasik ⁹⁷, A. Gautam ¹¹⁶, M.B. Gay Ducati ⁶⁵, M. Germain ¹⁰³, C. Ghosh¹³², M. Giacalone ²⁵, P. Giubellino ^{97,55}, P. Giubilato ²⁷, A.M.C. Glaenger ¹²⁸, P. Gläsel ⁹⁴, E. Glimos¹²⁰, D.J.Q. Goh⁷⁶, V. Gonzalez ¹³⁴, L.H. González-Trueba ⁶⁶, S. Gorbunov³⁸, M. Gorgon ², S. Gotovac³³, V. Grabski ⁶⁶, L.K. Graczykowski ¹³³, E. Grecka ⁸⁶, A. Grelli ⁵⁸, C. Grigoras ³², V. Grigoriev ¹⁴⁰, S. Grigoryan ^{141,1}, F. Grosa ³², J.F. Grosse-Oetringhaus ³², R. Grosso ⁹⁷, D. Grund ³⁵, G.G. Guardiano ¹¹¹, R. Guernane ⁷³, M. Guilbaud ¹⁰³, K. Gulbrandsen ⁸³, T. Gundem ⁶³, T. Gunji ¹²², W. Guo ⁶,

A. Gupta⁹¹, R. Gupta⁹¹, S.P. Guzman⁴⁴, L. Gyulai¹³⁶, M.K. Habib⁹⁷, C. Hadjidakis⁷², F.U. Haider⁹¹, H. Hamagaki⁷⁶, A. Hamdi⁷⁴, M. Hamid⁶, Y. Han¹³⁸, R. Hannigan¹⁰⁸, M.R. Haque¹³³, J.W. Harris¹³⁷, A. Harton⁹, H. Hassan⁸⁷, D. Hatzifotiadou⁵⁰, P. Hauer⁴², L.B. Havener¹³⁷, S.T. Heckel⁹⁵, E. Hellbär⁹⁷, H. Helstrup³⁴, M. Hemmer⁶³, T. Herman³⁵, G. Herrera Corral⁸, F. Herrmann¹³⁵, S. Herrmann¹²⁶, K.F. Hetland³⁴, B. Heybeck⁶³, H. Hillemanns³², C. Hills¹¹⁷, B. Hippolyte¹²⁷, B. Hofman⁵⁸, B. Hohlweger⁸⁴, G.H. Hong¹³⁸, M. Horst⁹⁵, A. Horzyk², R. Hosokawa¹⁴, Y. Hou⁶, P. Hristov³², C. Hughes¹²⁰, P. Huhn⁶³, L.M. Huhta¹¹⁵, C.V. Hulse⁷², T.J. Humanic⁸⁸, A. Hutson¹¹⁴, D. Hutter³⁸, J.P. Iddon¹¹⁷, R. Ilkaev¹⁴⁰, H. Ilyas¹³, M. Inaba¹²³, G.M. Innocenti³², M. Ippolitov¹⁴⁰, A. Isakov⁸⁶, T. Isidori¹¹⁶, M.S. Islam⁹⁹, M. Ivanov¹², M. Ivanov⁹⁷, V. Ivanov¹⁴⁰, M. Jablonski², B. Jacak⁷⁴, N. Jacazio³², P.M. Jacobs⁷⁴, S. Jadlovská¹⁰⁶, J. Jadlovsky¹⁰⁶, S. Jaelani⁸², L. Jaffe³⁸, C. Jahnke¹¹¹, M.J. Jakubowska¹³³, M.A. Janik¹³³, T. Janson⁶⁹, M. Jercic⁸⁹, S. Jia¹⁰, A.A.P. Jimenez⁶⁴, F. Jonas⁸⁷, J.M. Jowett^{32,97}, J. Jung⁶³, M. Jung⁶³, A. Junique³², A. Jusko¹⁰⁰, M.J. Kabus^{32,133}, J. Kaewjai¹⁰⁵, P. Kalinak⁵⁹, A.S. Kalteyer⁹⁷, A. Kalweit³², V. Kaplin¹⁴⁰, A. Karasu Uysal⁷¹, D. Karatovic⁸⁹, O. Karavichev¹⁴⁰, T. Karavicheva¹⁴⁰, P. Karczmarczyk¹³³, E. Karpechev¹⁴⁰, U. Kebschull⁶⁹, R. Keidel¹³⁹, D.L.D. Keijndener⁵⁸, M. Keil³², B. Ketzer⁴², A.M. Khan⁶, S. Khan¹⁵, A. Khanzadeev¹⁴⁰, Y. Kharlov¹⁴⁰, A. Khatun^{116,15}, A. Khuntia¹⁰⁷, M.B. Kidson¹¹³, B. Kileng³⁴, B. Kim¹⁶, C. Kim¹⁶, D.J. Kim¹¹⁵, E.J. Kim⁶⁸, J. Kim¹³⁸, J.S. Kim⁴⁰, J. Kim⁹⁴, J. Kim⁶⁸, M. Kim^{18,94}, S. Kim¹⁷, T. Kim¹³⁸, K. Kimura⁹², S. Kirsch⁶³, I. Kisel³⁸, S. Kiselev¹⁴⁰, A. Kisiel¹³³, J.P. Kitowski², J.L. Klay⁵, J. Klein³², S. Klein⁷⁴, C. Klein-Bösing¹³⁵, M. Kleiner⁶³, T. Klemenz⁹⁵, A. Kluge³², A.G. Knospe¹¹⁴, C. Kobdaj¹⁰⁵, T. Kollegger⁹⁷, A. Kondratyev¹⁴¹, N. Kondratyeva¹⁴⁰, E. Kondratyuk¹⁴⁰, J. Konig⁶³, S.A. Konigstorfer⁹⁵, P.J. Konopka³², G. Kornakov¹³³, S.D. Koryciak², A. Kotliarov⁸⁶, V. Kovalenko¹⁴⁰, M. Kowalski¹⁰⁷, V. Kozuharov³⁶, I. Králik⁵⁹, A. Kravčáková³⁷, L. Kreis⁹⁷, M. Krivda^{100,59}, F. Krizek⁸⁶, K. Krizkova Gajdosova³⁵, M. Kroesen⁹⁴, M. Krüger⁶³, D.M. Krupova³⁵, E. Kryshen¹⁴⁰, V. Kučera³², C. Kuhn¹²⁷, P.G. Kuijjer⁸⁴, T. Kumaoka¹²³, D. Kumar¹³², L. Kumar⁹⁰, N. Kumar⁹⁰, S. Kumar³¹, S. Kundu³², P. Kurashvili⁷⁹, A. Kurepin¹⁴⁰, A.B. Kurepin¹⁴⁰, A. Kuryakin¹⁴⁰, S. Kuschpil⁸⁶, J. Kvapil¹⁰⁰, M.J. Kweon⁵⁷, J.Y. Kwon⁵⁷, Y. Kwon¹³⁸, S.L. La Pointe³⁸, P. La Rocca²⁶, Y.S. Lai⁷⁴, A. Lakrathok¹⁰⁵, M. Lamanna³², R. Langoy¹¹⁹, P. Larionov³², E. Laudi³², L. Lautner^{32,95}, R. Lavicka¹⁰², T. Lazareva¹⁴⁰, R. Lea^{131,54}, H. Lee¹⁰⁴, G. Legras¹³⁵, J. Lehrbach³⁸, R.C. Lemmon⁸⁵, I. León Monzón¹⁰⁹, M.M. Lesch⁹⁵, E.D. Lesser¹⁸, M. Lettrich⁹⁵, P. Lévai¹³⁶, X. Li¹⁰, X.L. Li⁶, J. Lien¹¹⁹, R. Lietava¹⁰⁰, I. Likmeta¹¹⁴, B. Lim^{24,16}, S.H. Lim¹⁶, V. Lindenstruth³⁸, A. Lindner⁴⁵, C. Lippmann⁹⁷, A. Liu¹⁸, D.H. Liu⁶, J. Liu¹¹⁷, I.M. Lofnes²⁰, C. Loizides⁸⁷, S. Lokos¹⁰⁷, J. Lomker⁵⁸, P. Loncar³³, J.A. Lopez⁹⁴, X. Lopez¹²⁵, E. López Torres⁷, P. Lu^{97,118}, J.R. Luhder¹³⁵, M. Lunardon²⁷, G. Luparello⁵⁶, Y.G. Ma³⁹, A. Maevskaya¹⁴⁰, M. Mager³², T. Mahmoud⁴², A. Maire¹²⁷, M.V. Makariev³⁶, M. Malaev¹⁴⁰, G. Malfattore²⁵, N.M. Malik⁹¹, Q.W. Malik¹⁹, S.K. Malik⁹¹, L. Malinina^{VII,141}, D. Mal'Kevich¹⁴⁰, D. Mallick⁸⁰, N. Mallick⁴⁷, G. Mandaglio^{30,52}, V. Manko¹⁴⁰, F. Manso¹²⁵, V. Manzari⁴⁹, Y. Mao⁶, G.V. Margagliotti²³, A. Margotti⁵⁰, A. Marín⁹⁷, C. Markert¹⁰⁸, P. Martinengo³², J.L. Martínez¹¹⁴, M.I. Martínez⁴⁴, G. Martínez García¹⁰³, S. Masciocchi⁹⁷, M. Maserà²⁴, A. Masoni⁵¹, L. Massacrier⁷², A. Mastroserio^{129,49}, O. Matonoha⁷⁵, P.F.T. Matuoka¹¹⁰, A. Matyja¹⁰⁷, C. Mayer¹⁰⁷, A.L. Mazuecos³², F. Mazzaschi²⁴, M. Mazzilli³², J.E. Mdhuli¹²¹, A.F. Mechler⁶³, Y. Melikyan^{43,140}, A. Menchaca-Rocha⁶⁶, E. Meninno^{102,28}, A.S. Menon¹¹⁴, M. Meres¹², S. Mhlanga^{113,67}, Y. Miake¹²³, L. Micheletti⁵⁵, L.C. Migliorin¹²⁶, D.L. Mihaylov⁹⁵, K. Mikhaylov^{141,140}, A.N. Mishra¹³⁶, D. Miśkowiec⁹⁷, A. Modak⁴, A.P. Mohanty⁵⁸, B. Mohanty⁸⁰, M. Mohisin Khan^{V,15}, M.A. Molander⁴³, Z. Moravcova⁸³, C. Mordasini⁹⁵, D.A. Moreira De Godoy¹³⁵, I. Morozov¹⁴⁰, A. Morsch³², T. Mrnjavac³², V. Muccifora⁴⁸, S. Muhuri¹³², J.D. Mulligan⁷⁴, A. Mulliri²², M.G. Munhoz¹¹⁰, R.H. Munzer⁶³, H. Murakami¹²², S. Murray¹¹³, L. Musa³², J. Musinsky⁵⁹, J.W. Myrcha¹³³, B. Naik¹²¹, A.I. Nambrath¹⁸, B.K. Nandi⁴⁶, R. Nania⁵⁰, E. Nappi⁴⁹, A.F. Nassirpour⁷⁵, A. Nath⁹⁴, C. Nattrass¹²⁰, M.N. Naydenov³⁶, A. Neagu¹⁹, A. Negru¹²⁴, L. Nellen⁶⁴, S.V. Nesbo³⁴, G. Neskovic³⁸, D. Nesterov¹⁴⁰, B.S. Nielsen⁸³, E.G. Nielsen⁸³, S. Nikolaev¹⁴⁰, S. Nikulin¹⁴⁰, V. Nikulin¹⁴⁰, F. Noferini⁵⁰, S. Noh¹¹, P. Nomokonov¹⁴¹, J. Norman¹¹⁷, N. Novitzky¹²³, P. Nowakowski¹³³, A. Nyanin¹⁴⁰, J. Nystrand²⁰, M. Ogino⁷⁶, A. Ohlson⁷⁵, V.A. Okorokov¹⁴⁰, J. Oleniacz¹³³, A.C. Oliveira Da Silva¹²⁰, M.H. Oliver¹³⁷, A. Onnerstad¹¹⁵, C. Oppedisano⁵⁵, A. Ortiz Velasquez⁶⁴, J. Otwinowski¹⁰⁷, M. Oya⁹², K. Oyama⁷⁶, Y. Pachmayer⁹⁴, S. Padhan⁴⁶, D. Pagano^{131,54}, G. Paic⁶⁴, A. Palasciano⁴⁹, S. Panebianco¹²⁸,

H. Park¹²³, H. Park¹⁰⁴, J. Park⁵⁷, J.E. Parkkila³², R.N. Patra⁹¹, B. Paul²², H. Pei⁶,
T. Peitzmann⁵⁸, X. Peng⁶, M. Pennisi²⁴, L.G. Pereira⁶⁵, D. Peresunko¹⁴⁰, G.M. Perez⁷,
S. Perrin¹²⁸, Y. Pestov¹⁴⁰, V. Petráček³⁵, V. Petrov¹⁴⁰, M. Petrovici⁴⁵, R.P. Pezzi^{103,65}, S. Piano⁵⁶,
M. Pikna¹², P. Pillot¹⁰³, O. Pinazza^{50,32}, L. Pinsky¹¹⁴, C. Pinto⁹⁵, S. Pisano⁴⁸, M. Płoskoń⁷⁴,
M. Planinic⁸⁹, F. Pliquett⁶³, M.G. Poghosyan⁸⁷, B. Polichtchouk¹⁴⁰, S. Politano²⁹, N. Poljak⁸⁹,
A. Pop⁴⁵, S. Porteboeuf-Houssais¹²⁵, V. Pozdniakov¹⁴¹, K.K. Pradhan⁴⁷, S.K. Prasad⁴, S. Prasad⁴⁷,
R. Preghenella⁵⁰, F. Prino⁵⁵, C.A. Pruneau¹³⁴, I. Pshenichnov¹⁴⁰, M. Puccio³², S. Pucillo²⁴,
Z. Pugelova¹⁰⁶, S. Qiu⁸⁴, L. Quaglia²⁴, R.E. Quishpe¹¹⁴, S. Ragoni^{14,100}, A. Rakotozafindrabe¹²⁸,
L. Ramello^{130,55}, F. Rami¹²⁷, S.A.R. Ramirez⁴⁴, T.A. Rancien⁷³, M. Rasa²⁶, S.S. Räsänen⁴³,
R. Rath⁵⁰, M.P. Rauch²⁰, I. Ravasenga⁸⁴, K.F. Read^{87,120}, C. Reckziegel¹¹², A.R. Redelbach³⁸,
K. Redlich^{VI,79}, C.A. Reetz⁹⁷, A. Rehman²⁰, F. Reidt³², H.A. Reme-Ness³⁴, Z. Rescakova³⁷,
K. Reyers⁹⁴, A. Riabov¹⁴⁰, V. Riabov¹⁴⁰, R. Ricci²⁸, M. Richter¹⁹, A.A. Riedel⁹⁵,
W. Riegler³², C. Ristea⁶², M. Rodríguez Cahuantzi⁴⁴, K. Røed¹⁹, R. Rogalev¹⁴⁰, E. Rogochaya¹⁴¹,
T.S. Rogoschinski⁶³, D. Rohr³², D. Röhrich²⁰, P.F. Rojas⁴⁴, S. Rojas Torres³⁵, P.S. Rokita¹³³,
G. Romanenko¹⁴¹, F. Ronchetti⁴⁸, A. Rosano^{30,52}, E.D. Rosas⁶⁴, K. Roslon¹³³, A. Rossi⁵³,
A. Roy⁴⁷, S. Roy⁴⁶, N. Rubini²⁵, O.V. Rueda^{114,75}, D. Ruggiano¹³³, R. Rui²³, B. Rumyantsev¹⁴¹,
P.G. Russek², R. Russo⁸⁴, A. Rustamov⁸¹, E. Ryabinkin¹⁴⁰, Y. Ryabov¹⁴⁰, A. Rybicki¹⁰⁷,
H. Ryttonen¹¹⁵, W. Rzesza¹³³, O.A.M. Saarimaki⁴³, R. Sadek¹⁰³, S. Sadhu³¹, S. Sadovsky¹⁴⁰,
J. Saetre²⁰, K. Šafařík³⁵, S.K. Saha⁴, S. Saha⁸⁰, B. Sahoo⁴⁶, R. Sahoo⁴⁷, S. Sahoo⁶⁰, D. Sahu⁴⁷,
P.K. Sahu⁶⁰, J. Saini¹³², K. Sajdakova³⁷, S. Sakai¹²³, M.P. Salvan⁹⁷, S. Sambyal⁹¹, I. Sanna^{32,95},
T.B. Saramela¹¹⁰, D. Sarkar¹³⁴, N. Sarkar¹³², P. Sarma⁴¹, V. Sarritzu²², V.M. Sarti⁹⁵, M.H.P. Sas¹³⁷,
J. Schambach⁸⁷, H.S. Scheid⁶³, C. Schiaua⁴⁵, R. Schicker⁹⁴, A. Schmah⁹⁴, C. Schmidt⁹⁷,
H.R. Schmidt⁹³, M.O. Schmidt³², M. Schmidt⁹³, N.V. Schmidt⁸⁷, A.R. Schmier¹²⁰, R. Schotter¹²⁷,
A. Schröter³⁸, J. Schukraft³², K. Schwarz⁹⁷, K. Schweda⁹⁷, G. Scioli²⁵, E. Scomparin⁵⁵,
J.E. Seger¹⁴, Y. Sekiguchi¹²², D. Sekihata¹²², I. Selyuzhenkov^{97,140}, S. Senyukov¹²⁷, J.J. Seo⁵⁷,
D. Serebryakov¹⁴⁰, L. Šerkšnytė⁹⁵, A. Sevcenco⁶², T.J. Shaba⁶⁷, A. Shabetai¹⁰³, R. Shahoyan³²,
A. Shangaraev¹⁴⁰, A. Sharma⁹⁰, B. Sharma⁹¹, D. Sharma⁴⁶, H. Sharma¹⁰⁷, M. Sharma⁹¹,
S. Sharma⁷⁶, S. Sharma⁹¹, U. Sharma⁹¹, A. Shatat⁷², O. Sheibani¹¹⁴, K. Shigaki⁹², M. Shimomura⁷⁷,
J. Shin¹¹, S. Shirinkin¹⁴⁰, Q. Shou³⁹, Y. Sibiriak¹⁴⁰, S. Siddhanta⁵¹, T. Siemiarczuk⁷⁹,
T.F. Silva¹¹⁰, D. Silvermyr⁷⁵, T. Simantathammakul¹⁰⁵, R. Simeonov³⁶, B. Singh⁹¹, B. Singh⁹⁵,
R. Singh⁸⁰, R. Singh⁹¹, R. Singh⁴⁷, S. Singh¹⁵, V.K. Singh¹³², V. Singhal¹³², T. Sinha⁹⁹,
B. Sitar¹², M. Sitta^{130,55}, T.B. Skaali¹⁹, G. Skorodumovs⁹⁴, M. Slupecki⁴³, N. Smirnov¹³⁷,
R.J.M. Snellings⁵⁸, E.H. Solheim¹⁹, J. Song¹¹⁴, A. Songmoolnak¹⁰⁵, F. Soramel²⁷, R. Spijkers⁸⁴,
I. Sputowska¹⁰⁷, J. Staa⁷⁵, J. Stachel⁹⁴, I. Stan⁶², P.J. Steffanic¹²⁰, S.F. Stiefelmaier⁹⁴,
D. Stocco¹⁰³, I. Storehaug¹⁹, P. Stratmann¹³⁵, S. Strazzi²⁵, C.P. Stylianidis⁸⁴, A.A.P. Suaide¹¹⁰,
C. Suire⁷², M. Sukhanov¹⁴⁰, M. Suljic³², R. Sultanov¹⁴⁰, V. Sumberia⁹¹, S. Sumowidagdo⁸²,
S. Swain⁶⁰, I. Szarka¹², M. Szymkowski¹³³, S.F. Taghavi⁹⁵, G. Taillepied⁹⁷, J. Takahashi¹¹¹,
G.J. Tambave²⁰, S. Tang^{125,6}, Z. Tang¹¹⁸, J.D. Tapia Takaki¹¹⁶, N. Tapus¹²⁴, L.A. Tarasovicova¹³⁵,
M.G. Tarzila⁴⁵, G.F. Tassielli³¹, A. Tauro³², G. Tejeda Muñoz⁴⁴, A. Telesca³², L. Terlizzi²⁴,
C. Terrevoli¹¹⁴, G. Tersimonov³, S. Thakur⁴, D. Thomas¹⁰⁸, A. Tikhonov¹⁴⁰, A.R. Timmins¹¹⁴,
M. Tkacik¹⁰⁶, T. Tkacik¹⁰⁶, A. Toia⁶³, R. Tokumoto⁹², N. Topilskaya¹⁴⁰, M. Toppi⁴⁸,
F. Torres-Acosta¹⁸, T. Tork⁷², A.G. Torres Ramos³¹, A. Trifiró^{30,52}, A.S. Triolo^{30,52}, S. Tripathy⁵⁰,
T. Tripathy⁴⁶, S. Trogolo³², V. Trubnikov³, W.H. Trzaska¹¹⁵, T.P. Trzcinski¹³³, A. Tumkin¹⁴⁰,
R. Turrisi⁵³, T.S. Tveter¹⁹, K. Ullaland²⁰, B. Ulukutlu⁹⁵, A. Uras¹²⁶, M. Urioni^{54,131},
G.L. Usai²², M. Vala³⁷, N. Valle²¹, L.V.R. van Doremalen⁵⁸, M. van Leeuwen⁸⁴, C.A. van Veen⁹⁴,
R.J.G. van Weelden⁸⁴, P. Vande Vyvre³², D. Varga¹³⁶, Z. Varga¹³⁶, M. Vasileiou⁷⁸, A. Vasiliev¹⁴⁰,
O. Vázquez Doce⁴⁸, V. Vechernin¹⁴⁰, E. Vercellin²⁴, S. Vergara Limón⁴⁴, L. Vermunt⁹⁷,
R. Vértési¹³⁶, M. Verweij⁵⁸, L. Vickovic³³, Z. Vilakazi¹²¹, O. Villalobos Baillie¹⁰⁰, G. Vino⁴⁹,
A. Vinogradov¹⁴⁰, T. Virgili²⁸, V. Vislavicius⁷⁵, A. Vodopyanov¹⁴¹, B. Volkel³², M.A. Völkl⁹⁴,
K. Voloshin¹⁴⁰, S.A. Voloshin¹³⁴, G. Volpe³¹, B. von Haller³², I. Vorobyev⁹⁵, N. Vozniuk¹⁴⁰,
J. Vrláková³⁷, C. Wang³⁹, D. Wang³⁹, Y. Wang³⁹, A. Wegrzynek³², F.T. Weiglhofer³⁸, S.C. Wenzel³²,
J.P. Wessels¹³⁵, S.L. Weyhmiller¹³⁷, J. Wiechula⁶³, J. Wikne¹⁹, G. Wilk⁷⁹, J. Wilkinson⁹⁷,
G.A. Willems¹³⁵, B. Windelband⁹⁴, M. Winn¹²⁸, J.R. Wright¹⁰⁸, W. Wu³⁹, Y. Wu¹¹⁸, R. Xu⁶,
A. Yadav⁴², A.K. Yadav¹³², S. Yalcin⁷¹, Y. Yamaguchi⁹², S. Yang²⁰, S. Yano⁹², Z. Yin⁶,
I.-K. Yoo¹⁶, J.H. Yoon⁵⁷, S. Yuan²⁰, A. Yuncu⁹⁴, V. Zaccolo²³, C. Zampolli³², F. Zanone⁹⁴,
N. Zardoshti^{32,100}, A. Zarochentsev¹⁴⁰, P. Závada⁶¹, N. Zaviyalov¹⁴⁰, M. Zhalov¹⁴⁰, B. Zhang⁶,

L. Zhang ³⁹, S. Zhang ³⁹, X. Zhang ⁶, Y. Zhang¹¹⁸, Z. Zhang ⁶, M. Zhao ¹⁰, V. Zherebchevskii ¹⁴⁰,
Y. Zhi¹⁰, D. Zhou ⁶, Y. Zhou ⁸³, J. Zhu ^{97,6}, Y. Zhu⁶, S.C. Zugravel ⁵⁵, N. Zurlo ^{131,54}

Affiliation Notes

^I Deceased

^{II} Also at: Max-Planck-Institut für Physik, Munich, Germany

^{III} Also at: Italian National Agency for New Technologies, Energy and Sustainable Economic Development (ENEA), Bologna, Italy

^{IV} Also at: Dipartimento DET del Politecnico di Torino, Turin, Italy

^V Also at: Department of Applied Physics, Aligarh Muslim University, Aligarh, India

^{VI} Also at: Institute of Theoretical Physics, University of Wrocław, Poland

^{VII} Also at: An institution covered by a cooperation agreement with CERN

Collaboration Institutes

¹ A.I. Alikhanyan National Science Laboratory (Yerevan Physics Institute) Foundation, Yerevan, Armenia

² AGH University of Science and Technology, Cracow, Poland

³ Bogolyubov Institute for Theoretical Physics, National Academy of Sciences of Ukraine, Kiev, Ukraine

⁴ Bose Institute, Department of Physics and Centre for Astroparticle Physics and Space Science (CAPSS), Kolkata, India

⁵ California Polytechnic State University, San Luis Obispo, California, United States

⁶ Central China Normal University, Wuhan, China

⁷ Centro de Aplicaciones Tecnológicas y Desarrollo Nuclear (CEADEN), Havana, Cuba

⁸ Centro de Investigación y de Estudios Avanzados (CINVESTAV), Mexico City and Mérida, Mexico

⁹ Chicago State University, Chicago, Illinois, United States

¹⁰ China Institute of Atomic Energy, Beijing, China

¹¹ Chungbuk National University, Cheongju, Republic of Korea

¹² Comenius University Bratislava, Faculty of Mathematics, Physics and Informatics, Bratislava, Slovak Republic

¹³ COMSATS University Islamabad, Islamabad, Pakistan

¹⁴ Creighton University, Omaha, Nebraska, United States

¹⁵ Department of Physics, Aligarh Muslim University, Aligarh, India

¹⁶ Department of Physics, Pusan National University, Pusan, Republic of Korea

¹⁷ Department of Physics, Sejong University, Seoul, Republic of Korea

¹⁸ Department of Physics, University of California, Berkeley, California, United States

¹⁹ Department of Physics, University of Oslo, Oslo, Norway

²⁰ Department of Physics and Technology, University of Bergen, Bergen, Norway

²¹ Dipartimento di Fisica, Università di Pavia, Pavia, Italy

²² Dipartimento di Fisica dell'Università and Sezione INFN, Cagliari, Italy

²³ Dipartimento di Fisica dell'Università and Sezione INFN, Trieste, Italy

²⁴ Dipartimento di Fisica dell'Università and Sezione INFN, Turin, Italy

²⁵ Dipartimento di Fisica e Astronomia dell'Università and Sezione INFN, Bologna, Italy

²⁶ Dipartimento di Fisica e Astronomia dell'Università and Sezione INFN, Catania, Italy

²⁷ Dipartimento di Fisica e Astronomia dell'Università and Sezione INFN, Padova, Italy

²⁸ Dipartimento di Fisica 'E.R. Caianiello' dell'Università and Gruppo Collegato INFN, Salerno, Italy

²⁹ Dipartimento DISAT del Politecnico and Sezione INFN, Turin, Italy

³⁰ Dipartimento di Scienze MIFT, Università di Messina, Messina, Italy

³¹ Dipartimento Interateneo di Fisica 'M. Merlin' and Sezione INFN, Bari, Italy

³² European Organization for Nuclear Research (CERN), Geneva, Switzerland

³³ Faculty of Electrical Engineering, Mechanical Engineering and Naval Architecture, University of Split, Split, Croatia

³⁴ Faculty of Engineering and Science, Western Norway University of Applied Sciences, Bergen, Norway

³⁵ Faculty of Nuclear Sciences and Physical Engineering, Czech Technical University in Prague, Prague, Czech Republic

³⁶ Faculty of Physics, Sofia University, Sofia, Bulgaria

³⁷ Faculty of Science, P.J. Šafárik University, Košice, Slovak Republic

- ³⁸ Frankfurt Institute for Advanced Studies, Johann Wolfgang Goethe-Universität Frankfurt, Frankfurt, Germany
- ³⁹ Fudan University, Shanghai, China
- ⁴⁰ Gangneung-Wonju National University, Gangneung, Republic of Korea
- ⁴¹ Gauhati University, Department of Physics, Guwahati, India
- ⁴² Helmholtz-Institut für Strahlen- und Kernphysik, Rheinische Friedrich-Wilhelms-Universität Bonn, Bonn, Germany
- ⁴³ Helsinki Institute of Physics (HIP), Helsinki, Finland
- ⁴⁴ High Energy Physics Group, Universidad Autónoma de Puebla, Puebla, Mexico
- ⁴⁵ Horia Hulubei National Institute of Physics and Nuclear Engineering, Bucharest, Romania
- ⁴⁶ Indian Institute of Technology Bombay (IIT), Mumbai, India
- ⁴⁷ Indian Institute of Technology Indore, Indore, India
- ⁴⁸ INFN, Laboratori Nazionali di Frascati, Frascati, Italy
- ⁴⁹ INFN, Sezione di Bari, Bari, Italy
- ⁵⁰ INFN, Sezione di Bologna, Bologna, Italy
- ⁵¹ INFN, Sezione di Cagliari, Cagliari, Italy
- ⁵² INFN, Sezione di Catania, Catania, Italy
- ⁵³ INFN, Sezione di Padova, Padova, Italy
- ⁵⁴ INFN, Sezione di Pavia, Pavia, Italy
- ⁵⁵ INFN, Sezione di Torino, Turin, Italy
- ⁵⁶ INFN, Sezione di Trieste, Trieste, Italy
- ⁵⁷ Inha University, Incheon, Republic of Korea
- ⁵⁸ Institute for Gravitational and Subatomic Physics (GRASP), Utrecht University/Nikhef, Utrecht, Netherlands
- ⁵⁹ Institute of Experimental Physics, Slovak Academy of Sciences, Košice, Slovak Republic
- ⁶⁰ Institute of Physics, Homi Bhabha National Institute, Bhubaneswar, India
- ⁶¹ Institute of Physics of the Czech Academy of Sciences, Prague, Czech Republic
- ⁶² Institute of Space Science (ISS), Bucharest, Romania
- ⁶³ Institut für Kernphysik, Johann Wolfgang Goethe-Universität Frankfurt, Frankfurt, Germany
- ⁶⁴ Instituto de Ciencias Nucleares, Universidad Nacional Autónoma de México, Mexico City, Mexico
- ⁶⁵ Instituto de Física, Universidade Federal do Rio Grande do Sul (UFRGS), Porto Alegre, Brazil
- ⁶⁶ Instituto de Física, Universidad Nacional Autónoma de México, Mexico City, Mexico
- ⁶⁷ iThemba LABS, National Research Foundation, Somerset West, South Africa
- ⁶⁸ Jeonbuk National University, Jeonju, Republic of Korea
- ⁶⁹ Johann-Wolfgang-Goethe Universität Frankfurt Institut für Informatik, Fachbereich Informatik und Mathematik, Frankfurt, Germany
- ⁷⁰ Korea Institute of Science and Technology Information, Daejeon, Republic of Korea
- ⁷¹ KTO Karatay University, Konya, Turkey
- ⁷² Laboratoire de Physique des 2 Infinis, Irène Joliot-Curie, Orsay, France
- ⁷³ Laboratoire de Physique Subatomique et de Cosmologie, Université Grenoble-Alpes, CNRS-IN2P3, Grenoble, France
- ⁷⁴ Lawrence Berkeley National Laboratory, Berkeley, California, United States
- ⁷⁵ Lund University Department of Physics, Division of Particle Physics, Lund, Sweden
- ⁷⁶ Nagasaki Institute of Applied Science, Nagasaki, Japan
- ⁷⁷ Nara Women's University (NWU), Nara, Japan
- ⁷⁸ National and Kapodistrian University of Athens, School of Science, Department of Physics, Athens, Greece
- ⁷⁹ National Centre for Nuclear Research, Warsaw, Poland
- ⁸⁰ National Institute of Science Education and Research, Homi Bhabha National Institute, Jatni, India
- ⁸¹ National Nuclear Research Center, Baku, Azerbaijan
- ⁸² National Research and Innovation Agency - BRIN, Jakarta, Indonesia
- ⁸³ Niels Bohr Institute, University of Copenhagen, Copenhagen, Denmark
- ⁸⁴ Nikhef, National institute for subatomic physics, Amsterdam, Netherlands
- ⁸⁵ Nuclear Physics Group, STFC Daresbury Laboratory, Daresbury, United Kingdom
- ⁸⁶ Nuclear Physics Institute of the Czech Academy of Sciences, Husinec-Řež, Czech Republic
- ⁸⁷ Oak Ridge National Laboratory, Oak Ridge, Tennessee, United States
- ⁸⁸ Ohio State University, Columbus, Ohio, United States
- ⁸⁹ Physics department, Faculty of science, University of Zagreb, Zagreb, Croatia
- ⁹⁰ Physics Department, Panjab University, Chandigarh, India

- ⁹¹ Physics Department, University of Jammu, Jammu, India
⁹² Physics Program and International Institute for Sustainability with Knotted Chiral Meta Matter (SKCM2), Hiroshima University, Hiroshima, Japan
⁹³ Physikalisches Institut, Eberhard-Karls-Universität Tübingen, Tübingen, Germany
⁹⁴ Physikalisches Institut, Ruprecht-Karls-Universität Heidelberg, Heidelberg, Germany
⁹⁵ Physik Department, Technische Universität München, Munich, Germany
⁹⁶ Politecnico di Bari and Sezione INFN, Bari, Italy
⁹⁷ Research Division and ExtreMe Matter Institute EMMI, GSI Helmholtzzentrum für Schwerionenforschung GmbH, Darmstadt, Germany
⁹⁸ Saga University, Saga, Japan
⁹⁹ Saha Institute of Nuclear Physics, Homi Bhabha National Institute, Kolkata, India
¹⁰⁰ School of Physics and Astronomy, University of Birmingham, Birmingham, United Kingdom
¹⁰¹ Sección Física, Departamento de Ciencias, Pontificia Universidad Católica del Perú, Lima, Peru
¹⁰² Stefan Meyer Institut für Subatomare Physik (SMI), Vienna, Austria
¹⁰³ SUBATECH, IMT Atlantique, Nantes Université, CNRS-IN2P3, Nantes, France
¹⁰⁴ Sungkyunkwan University, Suwon City, Republic of Korea
¹⁰⁵ Suranaree University of Technology, Nakhon Ratchasima, Thailand
¹⁰⁶ Technical University of Košice, Košice, Slovak Republic
¹⁰⁷ The Henryk Niewodniczanski Institute of Nuclear Physics, Polish Academy of Sciences, Cracow, Poland
¹⁰⁸ The University of Texas at Austin, Austin, Texas, United States
¹⁰⁹ Universidad Autónoma de Sinaloa, Culiacán, Mexico
¹¹⁰ Universidade de São Paulo (USP), São Paulo, Brazil
¹¹¹ Universidade Estadual de Campinas (UNICAMP), Campinas, Brazil
¹¹² Universidade Federal do ABC, Santo Andre, Brazil
¹¹³ University of Cape Town, Cape Town, South Africa
¹¹⁴ University of Houston, Houston, Texas, United States
¹¹⁵ University of Jyväskylä, Jyväskylä, Finland
¹¹⁶ University of Kansas, Lawrence, Kansas, United States
¹¹⁷ University of Liverpool, Liverpool, United Kingdom
¹¹⁸ University of Science and Technology of China, Hefei, China
¹¹⁹ University of South-Eastern Norway, Kongsberg, Norway
¹²⁰ University of Tennessee, Knoxville, Tennessee, United States
¹²¹ University of the Witwatersrand, Johannesburg, South Africa
¹²² University of Tokyo, Tokyo, Japan
¹²³ University of Tsukuba, Tsukuba, Japan
¹²⁴ University Politehnica of Bucharest, Bucharest, Romania
¹²⁵ Université Clermont Auvergne, CNRS/IN2P3, LPC, Clermont-Ferrand, France
¹²⁶ Université de Lyon, CNRS/IN2P3, Institut de Physique des 2 Infinis de Lyon, Lyon, France
¹²⁷ Université de Strasbourg, CNRS, IPHC UMR 7178, F-67000 Strasbourg, France, Strasbourg, France
¹²⁸ Université Paris-Saclay Centre d'Etudes de Saclay (CEA), IRFU, Département de Physique Nucléaire (DPhN), Saclay, France
¹²⁹ Università degli Studi di Foggia, Foggia, Italy
¹³⁰ Università del Piemonte Orientale, Vercelli, Italy
¹³¹ Università di Brescia, Brescia, Italy
¹³² Variable Energy Cyclotron Centre, Homi Bhabha National Institute, Kolkata, India
¹³³ Warsaw University of Technology, Warsaw, Poland
¹³⁴ Wayne State University, Detroit, Michigan, United States
¹³⁵ Westfälische Wilhelms-Universität Münster, Institut für Kernphysik, Münster, Germany
¹³⁶ Wigner Research Centre for Physics, Budapest, Hungary
¹³⁷ Yale University, New Haven, Connecticut, United States
¹³⁸ Yonsei University, Seoul, Republic of Korea
¹³⁹ Zentrum für Technologie und Transfer (ZTT), Worms, Germany
¹⁴⁰ Affiliated with an institute covered by a cooperation agreement with CERN
¹⁴¹ Affiliated with an international laboratory covered by a cooperation agreement with CERN.